https://doi.org/10.5194/egusphere-2025-6305
Preprint. Discussion started: 12 January 2026

Jet Superposition and a Cut-off Low Behind a Rare Heavy Hailfall Episode in the United Arab Emirates (10–12 February 2024)

Noor AlShamsi[1], Micheal Weston[1], Ahmed Al Kaabi[1], Andrew VanderMerwe[2], and Alya Al Mazrouei[1]

[1]Research and Weather Enhancement Department, National Center of Meteorology, Abu Dhabi P.O. Box 4815, United Arab Emirates
[2]Technical Services Department, National Center of Meteorology, Abu Dhabi P.O. Box 4815, United Arab Emirates

Correspondence to: Noor AlShamsi (nalshamsi@ncm.gov.ae)

Abstract. Coupling between the polar and subtropical jet streams resulted in jet superposition and attendant upper-tropospheric divergence over the Arabian Peninsula, coincident with a southeastward-advancing Cut-Off Low (COL). On 12 February 2024, the associated convective system generated widespread, surface-verified hailfall across parts of the United Arab Emirates (UAE). This study examines the synoptic- and mesoscale evolution of this event using ECMWF operational analyses, CAMS reanalysis data, radiosonde soundings, satellite remote-sensing products, and radar-derived hail diagnostics. In view of the extensive regional dust plume present in the pre-convective environment, CAMS aerosol fields were analysed to assess the degree to which elevated dust layers modulated thermodynamic stability and moisture transport throughout the event. A COL developed south of Iraq, propagated southeastward, and subsequently interacted with a low-level baroclinic zone. Moisture advection from the Red Sea and the Arabian Sea was mediated by the Red Sea Trough (RST), thereby enhancing atmospheric instability. After an initial weakening stage, associated with mid-tropospheric drying and reduced low-level inflow, the convective system underwent re-intensification over the Arabian Gulf. Radiosonde observations from Abu Dhabi at 0000 UTC on 12 February indicated near-saturated conditions from the surface up to approximately 500 hPa, overlain by a comparatively dry mid-tropospheric layer. Concurrent EUMETSAT RGB composite imagery—optimized to depict dry-air intrusions and jet-related structures—exhibited upper-tropospheric signatures consistent with renewed deep convective development. Radar-derived hail products demonstrated that the period of most prolific hail production coincided with the convective system's mature stage, during which Hail Mass Aloft (HMA, > 100 kilotons) and Vertically Integrated Hail Mass (VIHM, > 2 kg m^{-2}) exceeded operational thresholds typically associated with a high probability of hail reaching the surface. The prevailing thermodynamic and microphysical environment was favourable for substantial hail deposition at the ground, whereas aerosol–radiation interactions appeared to be of secondary importance and did not exert a material influence on storm evolution relative to jet dynamics and moisture transport.

1 Introduction

This study examines how the interaction between the subtropical (STJ) and polar jet (PJ) streams, in conjunction with a southeastward-propagating cut-off low (COL), modulated moisture transport and vertical motion to generate an extreme hail

https://doi.org/10.5194/egusphere-2025-6305
Preprint. Discussion started: 12 January 2026

event over the United Arab Emirates (UAE) on 12 February 2024. Although hail occurrence is climatologically rare across the Arabian Peninsula (AP), characterizing its synoptic-scale forcing is critical for enhancing regional forecasting skill. Previous research has documented the influence of jet interactions and upper-tropospheric dynamical forcing on extreme precipitation over the Middle East (Nakamura et al., 2004; Steinhoff et al., 2018). However, the specific role of jet superposition (JSP) in organizing hail-producing convection within arid subtropical environments remains insufficiently quantified. The present case study provides the first explicit linkage between jet coupling, COL evolution, and independently verified surface hail reports over this region.

Jet streams emerge in regions characterized by strong meridional gradients in tropopause height and temperature, and they exert a fundamental influence on midlatitude circulation, particularly with respect to baroclinic development and cyclogenesis. While the STJ and PJ are usually distinguishable in terms of their latitudinal position and vertical structure, specific synoptic conditions can lead to their vertical alignment, resulting in the formation of a vertically consolidated jet core. This JSP is associated with enhanced divergence in the upper troposphere and an intensification of the ageostrophic circulation, thereby establishing a dynamically favorable environment for the occurrence of high-impact weather events (Christenson et al., 2017; Palmén & Newton, 1969; Winters & Martin, 2016).

Under specific synoptic configurations, the STJ and PJ can become vertically superposed, yielding a dynamically vigorous, vertically coherent jet structure. This JSP enhances upper-tropospheric divergence and associated ageostrophic circulations, thereby increasing the probability of rapid cyclogenesis and the occurrence of high-impact weather events (Christenson et al., 2017; Winters & Martin, 2016).

During the boreal winter, southeastward-propagating Mediterranean cyclones exert primary control over precipitation, extreme wind events, and aeolian dust transport across the northern AP. These synoptic-scale systems enhance low-level moisture advection from the Red Sea, the Mediterranean Sea, and the Arabian Gulf, while concurrently generating intense post-frontal winds that are sufficiently strong to initiate and sustain mineral dust entrainment and transport. The resulting circulation patterns thereby establish a robust dynamical framework that favors the co-occurrence of dust outbreaks and dynamically forced deep convection over the region (Almazroui et al., 2015; Francis et al., 2019; Houssos et al., 2015).

Wintertime dust plumes over the Arabian Peninsula can modulate convective processes through both radiative and microphysical mechanisms, including alterations to nocturnal boundary-layer stability and cloud microphysical properties when assimilated into mesoscale convective systems. Although dust–convection interactions have been investigated predominantly under summer or diurnal conditions, their influence on cold-season, nocturnal, hail-producing convective systems remains insufficiently characterized. This knowledge gap provides the primary motivation for incorporating dust-related diagnostics in the present case study (Farahat et al., 2015; Francis et al., 2021).

Despite these well-established synoptic-scale controls, most dust–convection research over the AP has concentrated on summertime or daytime radiative impacts. In contrast, cold-season, nocturnal dust stratification—particularly in association with convective inflow and hail-producing mesoscale convective systems (MCSs) along the eastern Gulf corridor—remains relatively unexplored. A systematic quantification of elevated (700–500 hPa) dust during such events, an assessment of its

https://doi.org/10.5194/egusphere-2025-6305
Preprint. Discussion started: 12 January 2026

nocturnal longwave radiative effects, and a diagnosis of the conditions under which dynamical processes outweigh aerosol-mediated mechanisms would directly address this critical knowledge gap.

Hail constitutes a high-impact, yet comparatively understudied, convective hazard across the eastern AP and the UAE. The region's arid, subtropical climate—characterized by pronounced subsidence, low annual precipitation, and substantial interannual and intraseasonal variability—reduces the frequency of hail occurrence and limits systematic surface documentation, thereby complicating both event confirmation and forecast verification (Airey et al., 2021). Under these conditions, hail production is frequently associated with synoptic-scale forcing mechanisms—such as upper-level jet interactions and jet superposition, COLs, and enhanced deep-layer vertical wind shear—rather than extreme convective available potential energy (CAPE) in isolation. To rigorously quantify hail frequency and the associated environments, we employ radar-derived hail diagnostics in conjunction with quality-controlled surface reports. Weather radar provides spatially continuous hail proxies that are well suited for climatological analyses in regions where in situ observations are sparse, and recent advances in dual-polarization radar and machine-learning-based algorithms have substantially improved the identification of severe hail (Allen et al., 2020; Forcadell et al., 2024).

In this case study, we examine the temporal and vertical evolution of atmospheric dust to assess whether nocturnal longwave radiative heating and elevated dust within the inflow layer modified thermodynamic stability, moisture transport, and cloud microphysical processes, or whether the hail-producing MCS was governed primarily by large-scale and mesoscale dynamical forcing. Clarifying this distinction facilitates more robust process-level attribution and enhances predictive capability in a region characterized by sparse in situ and remote-sensing observations.

This study investigates the synoptic-scale processes associated with a rare hail-producing convective episode over the UAE during 10–12 February 2024. The analysis focuses on the interaction between the STJ and PJ, the life cycle of an attendant COL, and the moisture-transport pathways that preconditioned and organized deep convection within an otherwise moisture-limited subtropical environment. By integrating reanalysis data, in situ observations, and weather radar measurements, we diagnose the extent to which large-scale dynamical forcing controlled storm initiation, evolution, and hail production. In addition, we evaluate the potential role of elevated wintertime dust as a secondary modulator of the thermodynamic environment. The methodologies and diagnostic approaches employed in this investigation are detailed in the subsequent sections.

2 Data and Methods

2.1 Study area and overview

The climate of the AP is predominantly characterized by a desert-type regime, featuring hot, dry summers and mild, comparatively wetter winters. According to the Köppen–Geiger climate classification, most of the AP is designated as a hot desert climate (BWh). In contrast, the southwestern sector exhibits a mild steppe climate, attributable to enhanced atmospheric convection and associated increases in precipitation (Abdullah & Al-Mazroui, 1998; Beck et al., 2018; Böer, 1997; Husain &

https://doi.org/10.5194/egusphere-2025-6305
Preprint. Discussion started: 12 January 2026

Chaudhary, 2008; Ragab & Prudhomme, 2000). Precipitation over the AP is typically sporadic and occurs in short-lived, high-intensity events, which frequently induce flash flooding and exert substantial adverse impacts on human populations, infrastructure, and natural ecosystems (Almazroui et al., 2012; Deng et al., 2015; Kumar et al., 2015). Rainfall is generally concentrated within brief temporal windows, ranging from hours to a few days, and is separated by prolonged dry spells lasting from several weeks to months, thereby reinforcing the hyper-arid character of the region.

The AP is influenced by four distinct climatological seasons: the northeast monsoon (December–March), the spring transitional period (April–May), the southwest monsoon (June–September), and the autumn transitional period (October–November). These seasonally varying regimes are modulated by large-scale atmospheric circulation systems, most notably the Indian summer monsoon to the south and synoptic-scale weather systems of Mediterranean origin to the north (Patlakas et al., 2019). The UAE, situated in the southeastern subtropical sector of the AP between 22.35°N–26.50°N and 51.35°E–57.10°E, is characterized by a distinct climatic regime. The country covers an area of approximately 71,024 km², comprising predominantly extensive sandy deserts and sabkha (salt flat) systems, with orographic features concentrated in the eastern and northeastern regions (Fig. 1a). The UAE has a population exceeding 10 million inhabitants. During the boreal summer, air temperatures in some regions frequently exceed 40 °C, whereas during winter nights—excluding the coastal fringe—temperatures may fall below 13 °C.

Although large-scale climatic modes such as the Indian summer monsoon and the El Niño–Southern Oscillation (ENSO) have been associated with long-term increases in winter precipitation over the eastern AP (Dasari et al., 2022), the UAE itself remains arid, receiving on average less than 120 mm of precipitation annually and exhibiting a mean cloud cover of only 24% (Yousef et al., 2019).

A 20-year climatological analysis (Nelli et al., 2021), employing ERA5 reanalysis data, satellite-derived infrared brightness temperature (IRBT), radar observations from the UAE, and radiosonde soundings, demonstrated that MCSs over the UAE have become increasingly long-lived. The study also documented a distinct seasonal cycle in MCS occurrence, with approximately 60% of events observed in spring (55% in March–April), 23% in winter, 12% in summer, and only 5% in autumn. Although recent investigations have examined convection associated with the Hajar Mountains using numerical model simulations (Branch et al., 2020; Fonseca et al., 2021, 2022, 2024; Gopalakrishnan et al., 2023; Schwitalla et al., 2020), there remains a paucity of research explicitly addressing the role of synoptic-scale systems in modulating hailstorm occurrence over the UAE.

https://doi.org/10.5194/egusphere-2025-6305
Preprint. Discussion started: 12 January 2026

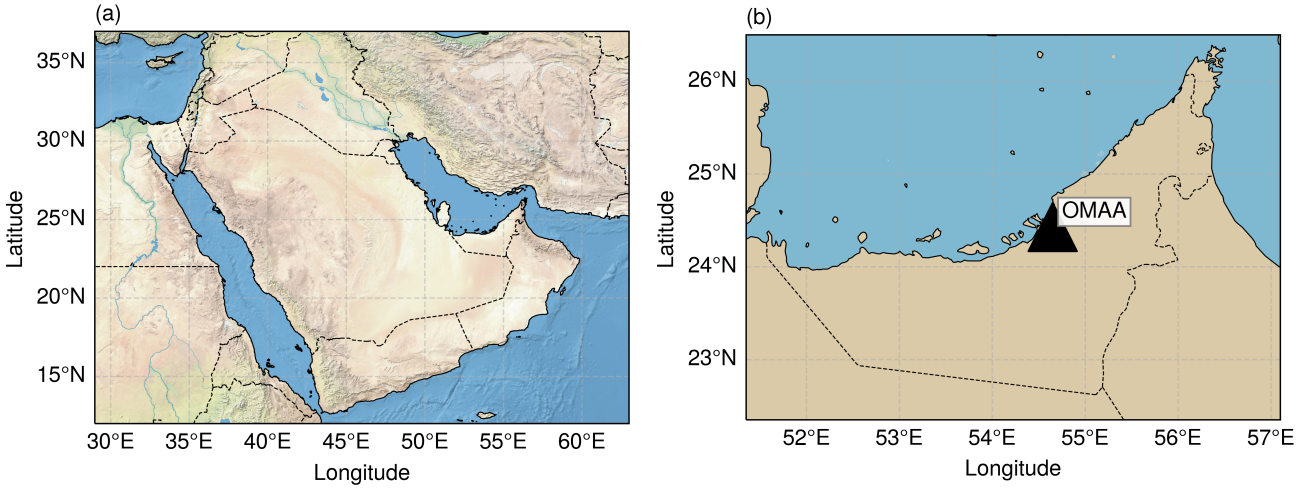

Figure 1. (a) Geographic map of the Arabian Peninsula (AP) with national borders overlaid; the red star marks the location of the United Arab Emirates (UAE). (b) Location of the UAE's operational radiosonde launch site at Abu Dhabi (Zayed) International Airport (OMAA; 24.430° N, 54.650° E), shown by a black triangle. The background is a terrain-shaded basemap for geographic context.

In addition to generating rainfall and hail, convective storms in the UAE are frequently associated with intense dust outbreaks, commonly referred to as haboobs. These phenomena develop when strong convective downdrafts impinge upon the surface, spread radially outward, and entrain unconsolidated desert sediments, thereby producing rapidly advancing dust fronts that substantially reduce horizontal visibility and enhance the overall hazard potential (Barbulescu & Nazzal, 2020; Miller et al., 2008; Nazzal et al., 2019; Saqer et al., 2024). Although the February 2024 event was noteworthy primarily for its extreme hail production, consideration of the broader climatological and environmental context of the AP's hyper-arid setting indicates that convective systems in this region commonly manifest as multi-hazard events, simultaneously involving precipitation, hail, and dust mobilization (Hamzeh et al., 2021; Marsham & Ryder, 2021; Solomos et al., 2017).

Between 10 and 12 February 2024, a deep convective system developed over the AP and, on 12 February, produced widespread, surface-verified hail across portions of the UAE. The event coincided with the southeastward propagation of a COL and the spatial superposition of the PJ and STJ, which together enhanced upper-tropospheric divergence. Concurrently, moisture was transported into the region via the RST. In the days preceding the event, a substantial, vertically extensive dust plume was present over central and northern Arabia, motivating an additional investigation into the extent to which dust-induced radiative and microphysical processes may have modified the evolving thermodynamic environment. Following a transient weakening phase associated with mid-tropospheric drying and reduced low-level inflow, deep convection reorganized over the Arabian Gulf late on 11 February and subsequently intensified into 12 February. Radar-derived hail diagnostics—HMA and VIHM—exceeded established operational thresholds during the mature stage of the system and corresponded well with independently confirmed surface hail reports, with the most severe impacts observed over central and eastern UAE. This

https://doi.org/10.5194/egusphere-2025-6305
Preprint. Discussion started: 12 January 2026

study examines the coupled dynamical, thermodynamic, and dust-aerosol processes that collectively governed this high-impact convective episode.

2.2 Data sources

2.2.1 ECMWF atmospheric model data

The High-Resolution 10-day Forecast (HRES, Set I) is a global numerical weather prediction system developed by the European Center for Medium-Range Weather Forecasts (ECMWF, Reading, United Kingdom). It assimilates a wide range of observational data, including satellite imagery, ground-based monitoring networks, Doppler radar measurements, and radiosonde profiles. The ECMWF-HRES operates at a horizontal grid spacing of 0.1° × 0.1°, delivering high-temporal-resolution forecasts of key atmospheric variables such as temperature, humidity, wind components, and precipitation. These forecasts have proven valuable for analyzing atmospheric evolution and for supporting the planning and management of major activities with substantial environmental and socioeconomic implications.

The ECMWF high-resolution forecast (HRES) system was configured with 137 hybrid sigma–pressure vertical levels, with the model top positioned at approximately 0.01 hPa. Although the model domain is global, all diagnostic fields were spatially confined to the region 0–50° N and 15–75° E. The analysis concentrated on the 00 UTC forecast cycle initialized on 10 February 2024, and model fields were examined through 13 February 2024. Forecast output was available at hourly intervals up to a lead time of +90 h, and at 3-hourly intervals thereafter up to +240 h. The HRES system is operated in a twice-daily cycle at 00 and 12 UTC.

The native HRES output (spatial resolution approximately 9 km, ~0.08°) was interpolated onto a regular 0.1° × 0.1° latitude–longitude grid using bilinear interpolation. All variables were constrained to the temporal and spatial extent of the event, converted to International System of Units (SI), and subsequently visualized employing a Plate Carrée map projection. In this study, the HRES dataset was selected over the course ERA5 reanalysis (0.25°), as its higher spatial resolution is better suited to resolving the fine-scale dynamical features associated with the event under investigation (Yang et al., 2022).

2.2.2 CAMS global reanalysis data

To examine the temporal evolution of regional dust loading preceding and during the event, we utilized aerosol fields from the Copernicus Atmosphere Monitoring Service (CAMS) global reanalysis, specifically the ECMWF Atmospheric Composition Reanalysis 4 (EAC4) (Inness et al., 2019). EAC4 is the fourth-generation ECMWF global reanalysis of atmospheric composition, produced with a four-dimensional variational (4D-Var) data assimilation scheme implemented in cycle CY42R1 of the Integrated Forecast System (IFS). The assimilation system employs 12-hour analysis windows (09–21 UTC and 21–09 UTC) on a global grid with a horizontal resolution of 0.75° × 0.75°. The vertical grid consists of 60 hybrid sigma–pressure model levels extending from the surface to 0.1 hPa. Atmospheric variables are provided on model levels and further interpolated to standard pressure, potential temperature (PT), and potential vorticity (PV) levels, in addition to single-level

https://doi.org/10.5194/egusphere-2025-6305
Preprint. Discussion started: 12 January 2026

near-surface diagnostic fields. The reanalysis output is available at a 3-hourly temporal resolution, which allows for a detailed characterization of the spatiotemporal evolution of dust. In this study, dust aerosol optical depth (AOD) at 550 nm was analyzed over the domain 32–65° E and 12–39° N.

Near-surface dust conditions were characterized using the coarse-mode dust aerosol (0.9–20 µm) mixing ratio (kg kg^{-1}) at the lowest available CAMS pressure level (1000 hPa). This diagnostic provides an estimate of the coarse dust mixing ratio within the boundary layer over the same spatial domain and temporal intervals as the layer-mean fields.

2.2.3 Spaceborne observations

To characterize the synoptic-scale and upper-tropospheric environment pertinent to the evolution of the event, this study employed Airmass RGB imagery from EUMETSAT's (Darmstadt, Germany) Meteosat-9 satellite. Meteosat-9 operates in the Indian Ocean Data Coverage (IODC) position at 45.5° E, providing full-disk coverage of the AP (Zavodsky et al., 2013). The Airmass RGB product was designed to facilitate the identification of large-scale atmospheric structures by offering a composite visualization of temperature and moisture contrasts across different tropospheric layers.

The Airmass RGB composite is generated using three infrared channels from the Spinning Enhanced Visible and Infrared Imager (SEVIRI): the 6.2 µm water vapor band, the 7.3 µm carbon dioxide band, and the 10.8 µm thermal infrared window channel. These channels are mapped to the red, green, and blue components of the composite image, respectively, thereby producing a multispectral depiction that enables discrimination among different air mass types. In this color scheme, dry stratospheric air, frequently associated with PV intrusions, is rendered in shades of red; moist mid- to upper-tropospheric air appears green; and cold post-frontal air masses are depicted in blue (*Airmass RGB Quick Guide | EUMETSAT - User Portal*, n.d.).

The Airmass RGB product is utilized here because it provides an especially effective tool for visualizing dry stratospheric intrusions and jet-level thermodynamic and kinematic gradients linked to PV streamers. This composite imagery supplies crucial synoptic-scale context for diagnosing jet coupling and the evolution of COLs, offering information that cannot be fully inferred from radiosonde measurements or from single-channel infrared (IR) observations alone. In the standard product, this channel exhibits an inversion in the temperature–radiance relationship over the range 243 K to 208 K, such that colder upper-tropospheric features are associated with higher measured radiances (i.e., they appear brighter in the imagery).

The SEVIRI instrument provides full-disk imagery every 15 minutes at the IODC position, with a nominal spatial resolution of approximately 4 km at nadir. This frequent 15-minute sampling interval, combined with the relatively high spatial resolution, renders the Airmass RGB product particularly effective for the detection and monitoring of upper-tropospheric and lower-stratospheric structures, including trough axes, jet streaks, and dry-air intrusions, all of which modulate the spatial distribution and temporal evolution of convective activity (Molthan et al., 2012). In the present study, the Airmass RGB product was employed to conduct a quantitative analysis of the spatial and temporal evolution of stratospheric air masses and PV streamers as they interacted over the AP, and to characterize the broader-scale dynamical environment conducive to storm development.

https://doi.org/10.5194/egusphere-2025-6305
Preprint. Discussion started: 12 January 2026

2.2.4 Radar data

Radar observations yield high-resolution, spatially and temporally continuous datasets that provide critical information on the structure, intensity, and lifecycle of convective storms, particularly in regions of the world with sparse in situ observational networks. Dual-polarization and Doppler weather radar systems enable three-dimensional characterization of storm systems through measurements of reflectivity, volumetric coverage, and radial velocity fields.

In the UAE, a national C-band, dual-polarimetric weather radar network comprising seven radars is operated by the National Center of Meteorology (NCM). Each radar operates at a wavelength of 5.3 cm with a beamwidth of 0.98°. Volume scans are performed every 6 minutes, providing coverage out to a range of 250 km. The radial range resolution is 150 m for three systems manufactured by Advanced Radar Company (Boulder, CO, USA) and 300 m for four systems manufactured by Vaisala (Vantaa, Finland).

Storm detection, tracking, and forecasting products are generated using the Lidar Radar Open Software Environment system (LROSE–Colette, version 2025; National Center for Atmospheric Research, Boulder, CO, USA) (DeHart et al., 2024). This framework incorporates an enhanced implementation of the Thunderstorm Identification, Tracking, Analysis, and Nowcasting (TITAN; NCAR, Boulder, CO, USA) algorithm (Dixon & Wiener, 1993; Han et al., 2009). A methodologically similar strategy was employed by Olivares & Jordan (2024), who examined a major rainfall event during January–February 2019 using radar-based storm tracking techniques.

Radar volume scans were processed using the TITAN algorithm, configured with a reflectivity threshold of 35 dBZ, a minimum storm volume of 20 km³, and a temporal update interval of 6 min, in alignment with NCM's operational specifications. The derived storm tracks and convective cell characteristics were subsequently assessed by comparison with corresponding products from ECMWF model analyses and satellite-based observations.

2.2.5 Upper air soundings

Radiosonde observations were conducted twice daily from Abu Dhabi (Zayed) International Airport (OMAA), the UAE's primary upper-air observation site (24.430° N, 54.650° E) (Fig. 1b). Atmospheric soundings, providing high-vertical-resolution profiles of temperature, dew point, pressure, and wind speed and direction from the surface to the lower stratosphere, were obtained at 0000 and 1200 UTC (0400 and 1600 local time) under the operational framework of the NCM. The observations employed the Vaisala RS41-SG radiosonde system (Vantaa, Finland), which is widely recognized for its high accuracy and reliability in characterizing thermodynamic and kinematic atmospheric structure. The launches routinely sampled the atmosphere to altitudes of approximately 30 km and form part of the WMO Integrated Global Upper-Air Observation Network (GUAN), thereby supplying data to the Global Telecommunication System (GTS). Globally disseminated quality-controlled profiles are accessible through the University of Wyoming upper-air archive (https://weather.uwyo.edu/upperair/sounding.html, accessed 17 Dec 2025), while full-resolution datasets are archived internally at NCM.

https://doi.org/10.5194/egusphere-2025-6305
Preprint. Discussion started: 12 January 2026

2.3 Diagnostics and definitions

Potential temperature (θ) was computed from temperature (T) on pressure level p using the dry-air Poisson relation (Eq. 1). Ertel PV from HRES is expressed in PV units (PVU; Eq. 2), and vertically integrated water vapor transport (IVT) was calculated from pressure-level humidity and winds following the standard definition (Eq. 3).

$$\theta = \mathrm{T}\left(\frac{p_0}{p}\right)^{\kappa}, \kappa = \frac{R}{c_p}, p_0 = 1000\ \mathrm{hPa}, \quad (1)$$

$$1\ \mathrm{PVU} = 10^{-6}\ \mathrm{K\ m^2\ kg^{-1}\ s^{-1}}, \quad (2)$$

$$\mathrm{IVT} = \sqrt{\left(\frac{1}{g}\int_{p_t}^{p_s} q\ u\ \mathrm{d}p\right)^2 + \left(\frac{1}{g}\int_{p_t}^{p_s} q\ v\ \mathrm{d}p\right)^2}, \quad (3)$$

Where R is the gas constant for dry air, c_p is the specific heat at constant pressure, g is gravitational acceleration, q is specific humidity, and u, v are the zonal and meridional wind components; p_s and p_t denote the lower and upper integration bounds (here, standard pressure levels spanning 1000-200 hPa).

From EAC4, we employed dust AOD at 550 nm to quantify the column-integrated dust burden, and the coarse-mode dust aerosol (0.9–20 µm) mixing ratio (kg kg^{-1}) to characterize its vertical distribution. To characterize the vertical distribution, we computed pressure-weighted, layer-mean coarse dust mixing ratios within three tropospheric layers: 1000–850 hPa, 850–700 hPa, and 700–500 hPa. For each pressure level p_i, the layer thickness Δp_i (Pa) was determined from the mid-level interfaces, and the layer-mean value was then calculated as

$$\bar{q}_{layer} = \frac{\sum_i q_i \Delta p_i}{\sum_i \Delta p_i}, \quad (4)$$

Where q_i denotes the dust mixing ratio at level p_i.

The Airmass RGB composite is generated from brightness temperature differences rather than from unprocessed channel radiances. In the standard EUMETSAT configuration for SEVIRI, the red component is computed as the difference between the 6.2 µm and 7.3 µm water vapor channels (WV6.2 − WV7.3). This difference is particularly sensitive to dry, ozone-enriched stratospheric intrusions that are typically collocated with anomalies in PV. The green component is derived from the difference between the ozone-sensitive 9.7 µm band and the 10.8 µm thermal infrared window channel (IR9.7 − IR10.8), thereby facilitating the discrimination between tropical and polar air masses. The blue component is obtained by applying an enhanced temperature stretch to the 6.2 µm water vapor brightness temperature.

TITAN is a radar-based object tracking algorithm that defines contiguous storm cells by applying reflectivity thresholds to 3D Cartesian gridded fields and then calculates a suite of storm-specific metrics (Raupach et al., 2021). These include storm-top height, maximum reflectivity, HMA, and VIHM based on reflectivity thresholds and vertical extent (Foote et al., 2005).

This study relied on two radar-derived hail diagnostics. HMA (ktons) estimates the total volume of hail suspended within a storm, providing insights into storm intensity and the efficiency of hail growth aloft. By contrast, VIHM (kg m^{-2}) represents

https://doi.org/10.5194/egusphere-2025-6305
Preprint. Discussion started: 12 January 2026

the column-integrated hail mass per unit area and is better suited to assessing the likelihood of hailstones reaching the surface. While HMA highlights vigorous hail production aloft, VIHM reveals whether that mass is vertically concentrated enough to survive descent. Used together, these parameters offer a complementary perspective, distinguishing storms that generate large hail volumes at height from those capable of producing damaging surface hail (Brimelow et al., 2002; Hulton & Schultz, 2024; Kunz et al., 2009; Pilorz & Łupikasza, 2020).

Radiosonde profiles were examined for atmospheric stability, moisture depth, and wind shear, as well as derived parameters such as CAPE, convective inhibition (CIN), and the lifting condensation level (LCL).

2.4 Quality control

For all observational datasets, standard quality-control procedures were implemented prior to analysis. Radiosonde profiles were first subjected to the Vaisala automated screening algorithms and subsequently inspected manually to detect potential artifacts in humidity, temperature, or wind measurements. No anomalous levels were identified in this study, and all soundings met the prescribed quality criteria. Radar reflectivity and radial-velocity measurements were processed using the standard NCM operational algorithms to remove ground clutter and non-meteorological echoes before application of the TITAN storm-tracking software. Numerical weather prediction and reanalysis products from ECMWF HRES and CAMS were systematically assessed for data completeness, spatial and temporal consistency, and adherence to standard meteorological sign conventions; no inconsistencies were detected. To ensure cross-dataset consistency, ECMWF-HRES fields for 15–16 April 2024 were extracted, horizontally interpolated to a 0.1° grid, and temporally collocated with radar and Automated Weather Stations (AWS) observations to maintain strict temporal alignment.

For the CAMS data, values below 0.1 were masked to de-emphasize very clear atmospheric conditions, and the plotted range (0.1–0.6) was chosen to highlight spatial gradients associated with moderate to high dust loadings during the event. The resulting fields were subsequently interpolated using bilinear interpolation onto a slightly higher-resolution latitude–longitude grid to mitigate pixelation artifacts in the visualizations. For clarity, the color scales were represented as $q \times 10^{-8}$ kg kg^{-1}.

For the Airmass RGB imagery, each color channel was normalized using the standard EUMETSAT scaling domains: approximately −26 K to +6 K for the water vapor channel difference, −4 K to +2 K for the ozone-sensitive brightness temperature difference, and 208 K to 243 K (inverted) for the enhanced 6.2 µm channel. Furthermore, gamma corrections were applied in the operational processing chain to optimize the perceptual discrimination among distinct air-mass types. Because these RGB composites are constructed from multispectral brightness temperature differences, the Airmass RGB product is intrinsically semi-quantitative: the resulting colour tones indicate relative thermodynamic contrasts rather than exact, absolute physical values. Accordingly, interpretation of Airmass RGB imagery is subject to several constraints, including sensitivity to satellite viewing geometry, cloud-top height, and the vertical weighting functions of the contributing spectral channels.

In this study, qualitative analysis of Airmass RGB features—such as dry intrusions, jet streaks, and PV streamer boundaries—was systematically supplemented with quantitative diagnostics (e.g., PV fields, upper-tropospheric wind analyses, and vertical thermodynamic profiles) to achieve a dynamically and thermodynamically consistent physical interpretation. To maintain

https://doi.org/10.5194/egusphere-2025-6305
Preprint. Discussion started: 12 January 2026

consistency with the UAE radar volume-scan schedule, Airmass RGB imagery was sampled at 15-min intervals, thereby establishing a one-to-one temporal correspondence between individual satellite images and radar volume scans over the entire lifetime of the event.

Despite persistent challenges associated with in situ hail measurements at the surface—particularly under mixed-phase precipitation conditions—TITAN's radar-derived hail diagnostics, most notably the Probability of Hail (POH) and VIHM, have demonstrated robust skill in reliably delineating hail-producing convective cells. As highlighted by Foote et al. (2005), the inherent difficulty in discriminating hail from rain at the surface is a primary motivation for emphasizing hail metrics derived aloft. Hail-related radar signatures are generally easier to detect and interpret at higher levels within the storm, in regions dominated by glaciogenic processes and ice-phase microphysics where hail growth is most pronounced.

Investigations conducted in Switzerland that employed exclusively reflectivity-based hail-detection schemes, anchored in Waldvogel et al. (1979)'s echo-top threshold criteria, have reported high-confidence identification of hail events (Delobbe & Holleman, 2006). Nonetheless, validation against independent datasets indicates that the skill and reliability of such algorithms can exhibit substantial regional variability (Kopp et al., 2024).

In this study, thresholds of 100 kilotons for HMA and 2 kg m^{-2} for VIHM were adopted because these values are employed operationally by the UAE's NCM to identify storms with a high probability of producing surface hail. Although a comprehensive and regionally representative validation dataset is not yet available for the UAE, these thresholds are deemed appropriate for local operational application, given the characteristics of the C-band radar network, the reflectivity–hail density relationships implemented in TITAN, and the climatological predominance of mixed-phase hail growth within Gulf cyclonic systems.

The principal sources of uncertainty include attenuation effects in regions of intense precipitation, assumptions inherent in the reflectivity-to-hail mass parameterization, and potential discontinuities in storm tracking. Nevertheless, sensitivity analyses reported in the literature indicate that the detection and classification of hail-producing storms are generally robust to these sources of error. Accordingly, the operational thresholds constitute a physically defensible and contextually appropriate framework for identifying storms capable of generating measurable surface hail in the UAE.

To independently assess the reliability of the hail diagnostics derived from radar observations, verified surface hail reports (Table A1) were collocated with the nearest TITAN storm object and its associated HMA and VIHM values. A spatial matching radius of 10 km and a temporal window of ±10 minutes were applied. The temporal tolerance was chosen to slightly exceed the 6-minute radar volume-scan interval to account for storm advection between successive scans as well as uncertainties in the reported hailfall times. For each hail report, the nearest peak in the radar-derived hail metrics was identified based on the trajectory of the storm centroid and the timing of the maximum hail intensity. All documented hailfall locations were linked to storm cells whose HMA and VIHM values exceeded the operational thresholds, thereby providing an observational consistency check between in situ hail occurrence and radar-inferred hail signatures.

In very dry atmospheric layers, which frequently occur over the Arabian Peninsula, the RS41 humidity sensor exhibits increased measurement uncertainty and a reduced response time. Consequently, humidity values below approximately 10%

https://doi.org/10.5194/egusphere-2025-6305
Preprint. Discussion started: 12 January 2026

relative humidity were treated as qualitative indicators of extremely arid conditions rather than as quantitatively robust measurements. Each radiosonde profile underwent a visual quality-control assessment to identify spurious humidity spikes, supersaturation artefacts, and sensor dropouts. No such anomalies were observed; therefore, no data levels were removed or adjusted.

3 Results

3.1 Synoptic overview and jet dynamics

The synoptic evolution of the storm over the AP during 10–12 February 2024 was strongly modulated by the interaction between the PJ and the STJ, a configuration commonly referred to as JSP. The JSP was established from the East African sector across the central AP, thereby providing a dynamically favorable environment for storm development. The coupling of the upper-tropospheric jets is known to enhance vertical motions and upper-level divergence, both of which are critical for the initiation and intensification of cyclonic systems (Kunz et al., 2020). Polar-jet–dominant JSP substantially increases thermal instability and vertical wind shear, thereby elevating the likelihood of severe storm formation (Yamane & Hayashi, 2006). In this case, the jet configuration fostered conditions conducive to cyclogenesis, as the strong upper-level winds and increased flow curvature over the northwestern AP promoted the amplification of elevated PV anomalies aloft, supporting the subsequent development and organization of the storm system.

The 300-hPa geopotential height and wind fields (Fig. 2a) at 0200 UTC on 11 February exhibit a well-defined jet streak pattern, while the corresponding PV fields (Fig. 2b) reveal a filament of high-PV air descending from the lower stratosphere into the upper troposphere over the study region, consistent with upper-tropospheric subsidence and baroclinic forcing. This PV filament enhanced cyclonic relative vorticity in the mid-troposphere, thereby promoting dynamical instability and upward motion. The JSP further contributed to an environment characterized by amplified cyclonic vorticity and increased atmospheric instability.

The anomalously elevated PV in the upper troposphere–lower stratosphere acted as a key dynamical mechanism for storm intensification. The presence of high-PV air in the near-tropopause region modifies the thermodynamic structure in a manner that effectively increases static instability and facilitates upward vertical motion through the release of conditional instability (Galarneau et al., 2010; Riemer & Montgomery, 2011). This configuration is frequently associated with tropopause folding, which injects stratospheric high-PV air into the upper troposphere, thereby strengthening baroclinic instability and promoting enhanced cyclogenesis (Thompson et al., 2018).

https://doi.org/10.5194/egusphere-2025-6305
Preprint. Discussion started: 12 January 2026

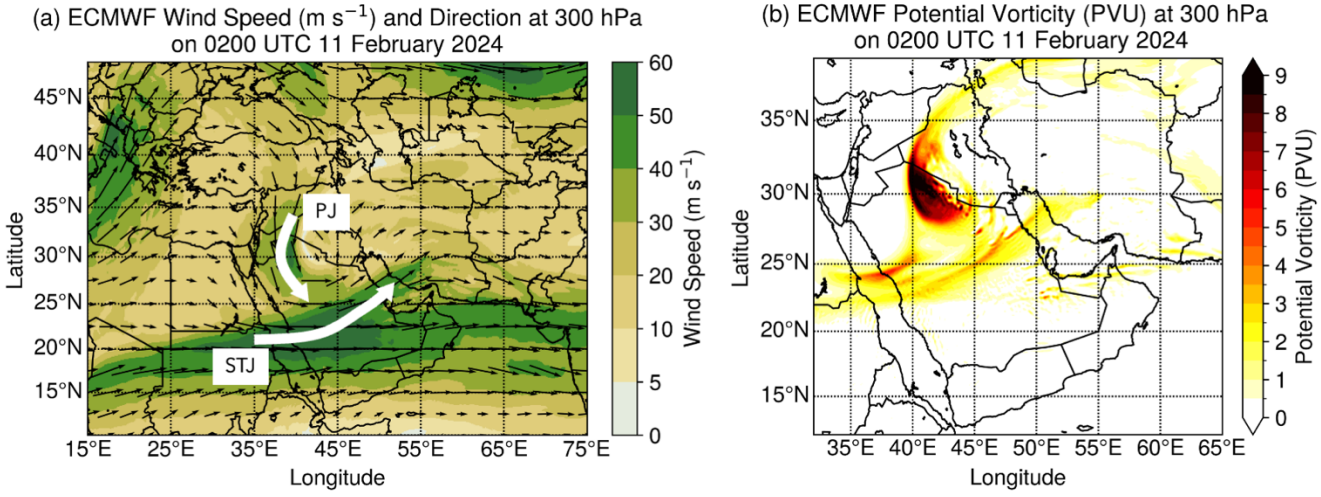

Figure 2. ECMWF analysis at 300 hPa at 0200 UTC on 11 February 2024: (a) Wind speed (shading, m s⁻¹) and direction (vectors), illustrating pronounced upper-tropospheric jet streams; additional arrows denote the jet streak position of both the subtropical jet (STJ) and the polar jet (PJ) over the AP. (b) Potential vorticity (PV, PVU), emphasizing a descending, high-PV filament over northern Saudi Arabia and Iraq, indicative of upper-level subsidence and baroclinic forcing that collectively favor cyclogenesis.

These processes contribute to the maintenance of elevated near-surface moisture by limiting dewpoint depression, thereby promoting convective development. They may also enhance dryline bulging, wherein intensified low-level convergence along the dryline boundary augments vertical motion. Although high PV intrusions do not directly reduce the LCL, they impart stronger dynamic forcing in the upper troposphere. This additional ascent, when superimposed on a moist boundary layer, can serve as an effective triggering mechanism for deep convection (Bhate et al., 2016). In the present case, the establishment of a COL further amplified these processes, sustaining vertical instability and prolonging convective storm activity.

3.2 Frontal structure and cyclone evolution

Satellite-based airmass RGB imagery (Fig. 3), constructed following the methodology of Tsironis et al. (2023), depicts a dry, stratospheric intrusion wrapping cyclonically into the synoptic system. This feature constitutes a clear signature of baroclinic development and trough intensification. The upper-tropospheric dynamical forcing coincided with the formation of a COL over the Fertile Crescent at 1300 UTC 10 February. The COL, diagnosed by the presence of closed isobars at upper levels, acted to concentrate synoptic-scale ascent and thereby facilitated the continued cyclonic deepening of the system.

Upper-tropospheric flow advected the system southeastward toward the AG, enhancing synoptic-scale upward motion and facilitating the formation of an intense surface cyclone. Consistent with the cases documented by Mazza et al. (2017) and Mohammed Abdul Raheem Jabbar & Ahmad S. Hassan (2022), the COL preserved a deep vertical structure, which enabled effective vertical momentum transport and sustained thermodynamic support throughout the entire tropospheric column. This dynamical configuration led to a further intensification of the storm and expanded its spatial extent and regional impact.

https://doi.org/10.5194/egusphere-2025-6305
Preprint. Discussion started: 12 January 2026

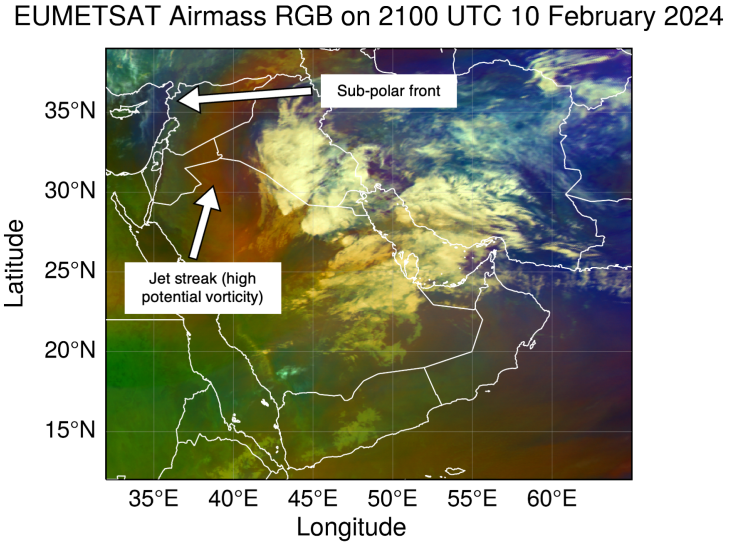

Figure 3. EUMETSAT Meteosat-9 Airmass RGB imagery (IODC, 45.5° E) at 2100 UTC on 10 February 2024 documents the upper-tropospheric flow configuration over northeastern Africa and the eastern Mediterranean. The orange–brown shading denotes regions of stratospheric air intrusions, and an embedded jet streak associated with enhanced PV, while the dark blue band marks the position of the subpolar frontal zone. Collectively, these signatures delineate the interaction region between the PJ and STJ, consistent with the onset of JSP and with pronounced upper-level dynamical forcing in advance of the developing cyclonic system.

The cyclonic circulation associated with the COL established a well-defined subpolar cold frontal zone extending across the AP. This frontal structure enhanced low-level convergence and vertical ascent, as evidenced by the PT field at 700 hPa (Fig. 4a). It delineated a sharp thermodynamic boundary between warm, moist air in the pre-frontal sector and cold, dry air in the post-frontal environment. The pronounced thermal contrast between these air masses produced strong horizontal temperature gradients and induced baroclinic instability through vertically coherent motion, thereby promoting the initiation, organization, and intensification of deep convection and thunderstorms. The cold front, wrapping cyclonically around the low-pressure center, acted as a primary dynamical mechanism for triggering ascent and convective development along and immediately ahead of its boundary.

https://doi.org/10.5194/egusphere-2025-6305
Preprint. Discussion started: 12 January 2026

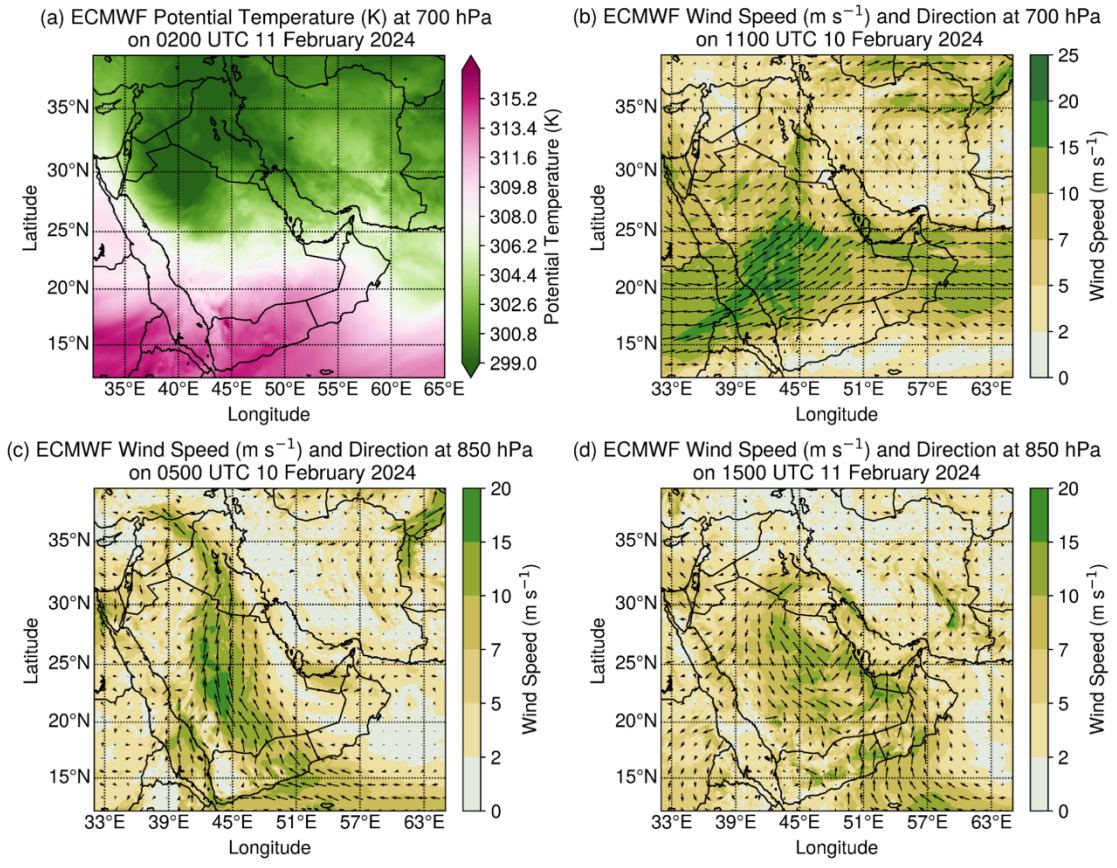

Figure 4. ECMWF reanalysis fields depicting the evolving thermal structure and wind flow during the initial phase of system development on 10–11 February 2024. (a) 700-hPa potential temperature (K) at 0200 UTC on 11 February, illustrating a pronounced baroclinic zone extending across the central AP. (b) 700-hPa wind speed and direction at 1100 UTC on 10 February, indicating mid-tropospheric south-westerly flow that advected warm, moist air from the Red Sea and Arabian Sea northward into the system's warm sector. (c) 850-hPa wind vectors at 0500 UTC on 10 February, showing the onset of low-level moisture transport from the Arabian Sea and Red Sea. (d) 850-hPa winds at 1500 UTC on 11 February, demonstrating the persistence of low-level inflow from the Red Sea and Arabian Sea. This sustained inflow maintained a continuous supply of warm, moist air into the storm's warm sector, thereby supporting ongoing convection and enhancing baroclinic intensification.

3.3 Moisture transport pathways and system initiation

The RST exerted a pronounced influence during the early stage of cyclogenesis by establishing a zone of low-level convergence that enhanced moisture transport into the cyclone's inflow region. In addition, the RST modulated both the timing and the intensity of the initial convective development, thereby preconditioning the environment for subsequent intensification as upper-tropospheric disturbances approached. Functionally, it acted as a moisture conduit, augmenting the influx of humid air along the system's trajectory from the Red Sea and adjacent regions.

The deep-layer wind field at 500, 700, and 850 hPa (Fig. 4b–d) favored poleward moisture advection into the warm sector of the cyclone. Mid- and lower-tropospheric winds facilitated moisture transport from both the Red Sea and the Arabian Sea, supplying the developing system with latent heat crucial for intensification. As this moisture underwent condensation, the

https://doi.org/10.5194/egusphere-2025-6305
Preprint. Discussion started: 12 January 2026

associated latent heat release amplified the environmental baroclinicity and promoted convective initiation. The convergence of these moisture fluxes increased precipitable water content and enhanced atmospheric instability, collectively creating a thermodynamically favorable environment for storm development. Although the RST constituted the primary pathway for moisture transport, low-level southerly flow from the Arabian Sea provided an additional moisture source to the storm's warm sector, consistent with the monsoonal inflow documented in previous studies.

Multiple air mass trajectories contributed to the transport of moist air into the storm's warm sector. Low-level flow advected moisture from the Red Sea Basin via the RST, while mid-tropospheric circulation transported additional moisture from the Arabian Sea Basin. The presence of these moisture-bearing streamlines ahead of the cyclone core substantially enhanced the potential for deep convection along and downstream of the frontal zone. This moisture transport can be conceptualized as an "air conditioning" mechanism that intensifies surface evaporation, increases latent heat uptake, and thereby fosters further atmospheric destabilization (Trenberth & Shea, 2005). Since aerosols can modulate both the radiative and microphysical properties of such an environment, we examine the corresponding temporal evolution of mineral dust using CAMS diagnostics in Section 3.5.

3.4 Lifecycle of convective activity

As the system approached the AG, it underwent a transient weakening phase attributable to reduced low-level moisture advection and the presence of a persistent mid-tropospheric capping inversion. As the moisture available to support deep convection diminished, the convective organization became increasingly fragmented and lost structural coherence. This reduction in moisture transport is evident in the ECMWF-derived IVT fields, which display a pronounced decrease in integrated water vapor flux into the central and northern AP during the interval from 1400 UTC 10 February to 1300 UTC 11 February (Fig. 5a–b). Although this weakening was short-lived, the synoptic-scale evolution became increasingly favorable for renewed cyclogenesis as the cyclone propagated eastward over Kuwait. By 0000 UTC 12 February, radiosonde observations at OMAA indicated substantial low-level moistening extending from the surface up to 500 hPa (Fig. 6), with near-surface saturation, consistent with AG–sourced moisture intruding into a previously dry mid-tropospheric layer.

EUMETSAT Airmass RGB imagery at 1330 and 2300 UTC on 11 February (Fig. 7a–b) documented the presence of a well-organized convective band that subsequently evolved into a MCS over the central AG. This convective regeneration occurred under a favorable synoptic-scale configuration in which the UAE was situated within the left-exit region of the STJ, a sector typically associated with enhanced upper-tropospheric divergence.

The timing and structural evolution of the convective cells indicate that the convective intensification was primarily driven by increased vertical moisture continuity in conjunction with dynamically conducive upper level forcing. Although midlevel lapse rates may have been modified during the preceding drying phase, there is no compelling evidence that aerosol-induced microphysical processes became the dominant control on storm evolution. Instead, the redevelopment of deep convection appears to have been sustained by adequate thermodynamic organization and robust large-scale dynamical forcing.

https://doi.org/10.5194/egusphere-2025-6305
Preprint. Discussion started: 12 January 2026

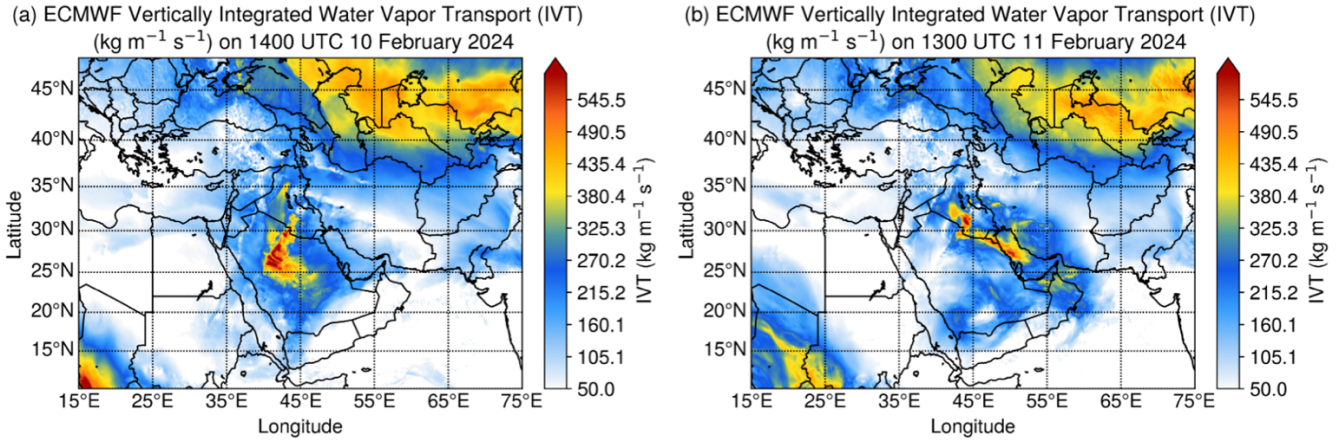

Figure 5. ECMWF vertically integrated water vapor transport (IVT, kg m^{-1} s^{-1}) illustrating the moisture flux into the AP. (a) At 1400 UTC on 10 February 2024, a pronounced southwesterly IVT is evident across the Red Sea and central AP, indicative of efficient moisture advection into the warm sector of the storm. (b) By 1300 UTC on 11 February 2024, the IVT directed toward the central and northern AP has weakened substantially, implying a marked reduction in low-level moisture transport, consistent with the observed decline in convective activity.

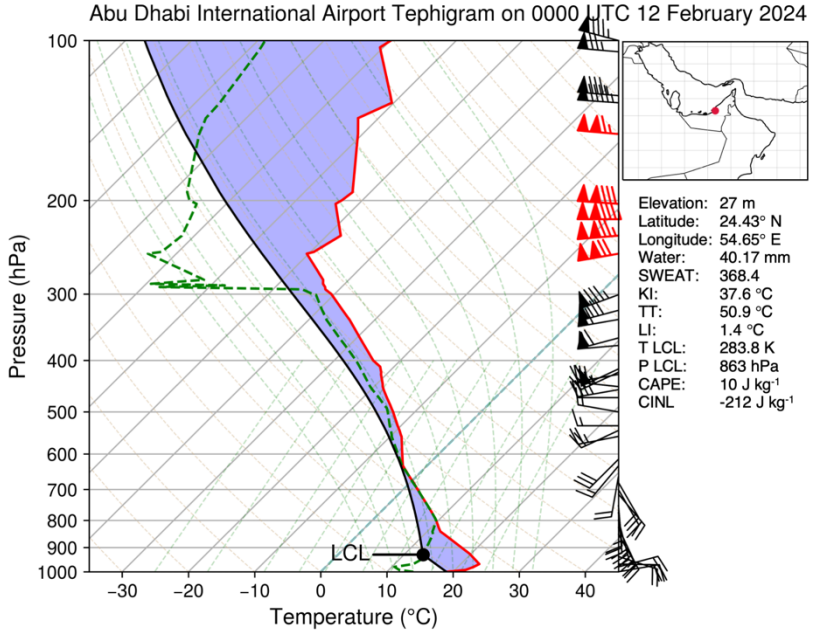

Figure 6. Tephigram from OMAA at 0000 UTC on 12 February 2024 displaying the vertical temperature profile (red curve), dew point profile (blue curve), and the Lifted Condensation Level (LCL). The shaded region delineates the layer of positive Convective Available Potential Energy (CAPE ≈ 11.3 J kg^{-1}), while substantial Convective Inhibition (CIN ≈ −211.7 J kg^{-1}) is also present, indicating a strongly capped thermodynamic environment that is unfavorable for surface-based deep convection. Nevertheless, the elevated value of the Severe Weather Threat (SWEAT) index (368.4), combined with pronounced vertical wind shear in the mid- to upper troposphere, suggests an environment conducive to elevated convective development and hail production, in agreement with concurrent radar observations.

https://doi.org/10.5194/egusphere-2025-6305
Preprint. Discussion started: 12 January 2026

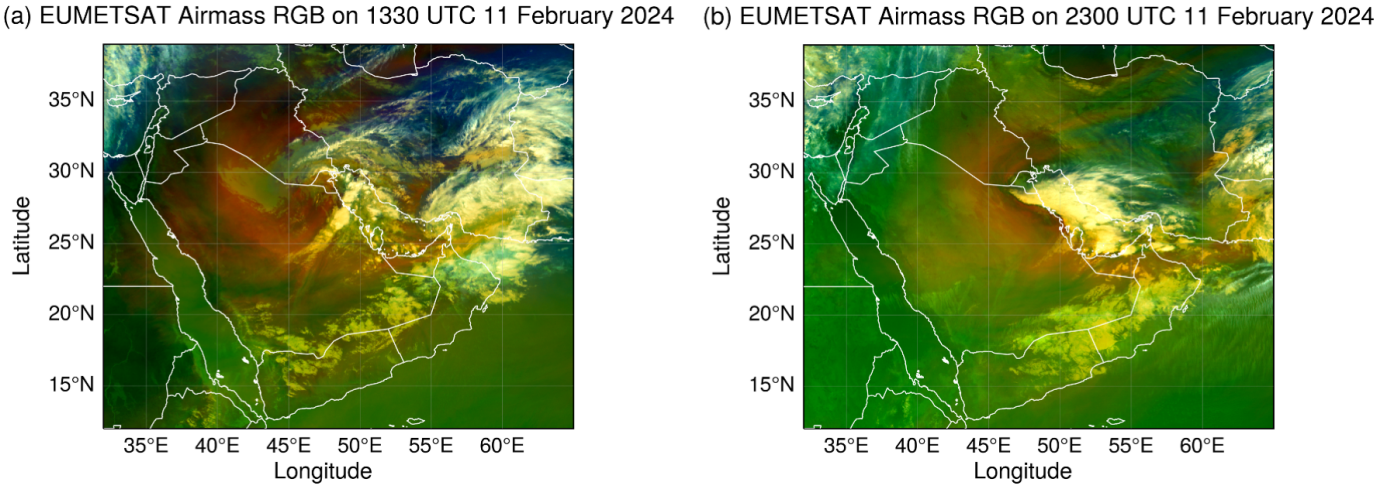

Figure 7. EUMETSAT Meteosat-9 Airmass RGB imagery (IODC, 45.5° E) depicting the evolution of upper-tropospheric dynamics and convective organization on 11 February 2024. (a) At 1330 UTC, a well-defined comma-head cloud configuration is evident over the central AP, characterized by pronounced magenta and reddish hues that are diagnostic of intrusions of dry, stratospherically influenced air and the cyclonic wrapping of upper-level PV into the system. (b) By 2300 UTC, a region of organized deep convection has substantially intensified over the central AG and the UAE, concurrent with enhanced upper-tropospheric divergence and renewed low-level moisture availability, signifying the transition toward a mature mesoscale convective system.

To further characterize the instability environment, several diagnostic indices were computed from the 00Z Abu Dhabi radiosonde profile. The Severe Weather Threat (SWEAT) Index (368.4) indicated a pronounced potential for severe convective phenomena, consistent with radar observations of hail. The K-Index (37.6) suggested a high probability of thunderstorm occurrence under moist, conditionally unstable conditions, while the Total Totals Index (50.9) corroborated the presence of substantial instability conducive to organized deep convection. In contrast, the CAPE Index (11.3 J kg^{-1}) was very low, implying that surface-based convection was unlikely. Nevertheless, when considered in conjunction with strong vertical wind shear, elevated SWEAT values, and enhanced moisture transport, the composite thermodynamic and kinematic environment was supportive of elevated convection, consistent with the observed storm intensity and associated hail production.

3.5 Dust distribution and aerosol–dynamic interactions

Prior to the full maturation of the cyclone, CAMS diagnostics indicate that a vertically extensive mineral dust plume was already established over central and northern Arabia. The total column dust burden locally exceeded approximately 0.9×10^{-3} kg m^{-2}, with dust AOD values on the order of 0.5–0.6 over portions of central Saudi Arabia (Fig. 8a–b). This deep, elevated, and surface-coupled plume weakened downwelling shortwave radiation at the surface and induced tropospheric warming, thereby enhancing static stability and effectively capping the planetary boundary layer. Such conditions are conducive to the suppression of shallow convection while simultaneously strengthening horizontal thermal gradients.

The resulting dust-driven radiative heating and stabilization can intensify mesoscale circulations and modulate moisture transport from the Arabian Sea, thus preconditioning the environment for subsequent convective initiation once strong

https://doi.org/10.5194/egusphere-2025-6305
Preprint. Discussion started: 12 January 2026

synoptic-scale ascent develops. As the upper-tropospheric jet structure and the associated COL intensified, the dust plume became more vertically elevated and increasingly constrained by the large-scale dynamics (Fig. 8c). The analyses further indicate that dust loading decreased over western Saudi Arabia and increased over eastern Saudi Arabia and the northern AG, consistent with the reorganization of southwesterly and westerly flow ahead of the PV filament.

Under this configuration, the bulk of the dust mass was embedded within the lower- to mid-tropospheric inflow rather than being confined to the near-surface layer. This vertical redistribution permitted modest differential radiative heating aloft, while exerting only a limited direct influence on boundary-layer thermodynamics. Consequently, dust acted primarily as a secondary modulator of the jet–frontal environment, whereas the evolution of the PV streamer and COL remained controlled predominantly by synoptic-scale dynamical processes.

Following the onset of organized deep convection, the vertical distribution of atmospheric dust underwent a marked reconfiguration. Layer-mean CAMS analyses reveal a decrease in dust mass concentrations at upper levels and a concurrent enhancement of near-surface dust loading over segments of eastern Saudi Arabia, Qatar, and the western AG (Fig. 8d–e). This spatial signature is consistent with the downward mixing of an initially elevated dust plume mediated by turbulent entrainment, convective downdrafts, and wet scavenging associated with clouds and precipitation.

Elevated dust layers are efficient absorbers of shortwave radiation and typically contribute to the stabilization of the mid-troposphere. Following the downward mixing and dilution of this dust, its stabilizing radiative effect is substantially reduced. The documented vertical redistribution of dust therefore constitutes a physically plausible mechanism for the observed transition from a comparatively slowly evolving, dust-stabilized regime to a more dynamically active convective phase, in which baroclinic processes play a central role.

During the subsequent daytime weakening phase, a reduction in low-level moisture transport into the cyclone inflow region coincided with enhanced atmospheric dust loading over portions of Qatar, western UAE, and eastern Saudi Arabia. Under weakened wet scavenging conditions, dust concentrations became more pronounced throughout the vertical column. During daylight hours, this additional elevated dust layer can further warm the mid-troposphere and attenuate surface shortwave radiation reaching the surface, thereby reinforcing the midlevel capping inversion that develops in response to moisture depletion. In this manner, dust exerted a radiative modulation on the convective lull, amplifying the suppressive effects of the moisture deficit; however, it did not independently control the weakening of the system.

By evening, atmospheric dust loading decreased once more along the principal convective corridor extending from the northern AG toward the UAE, with the most substantial reduction observed within the mid-troposphere. The attenuation of the elevated dust layer weakened the radiatively absorbing “cap” that had previously contributed to enhanced midlevel warming and a reduction in surface-incident solar radiation. As the concentration of dust aloft declined, static stability was reduced, deep-layer ascent along the low-level inflow pathway intensified, and the combined thermodynamic and dynamical environment became increasingly favorable for renewed convective initiation and development. This temporal evolution of the dust distribution coincided with the re-establishment of upper-tropospheric divergence and enhanced moisture advection, indicating

https://doi.org/10.5194/egusphere-2025-6305
Preprint. Discussion started: 12 January 2026

that although dust may have exerted a modest stabilizing influence during the re-intensification phase, the dominant controls on storm redevelopment were associated with upper-level jet coupling and the restoration of low- to mid-tropospheric moisture.

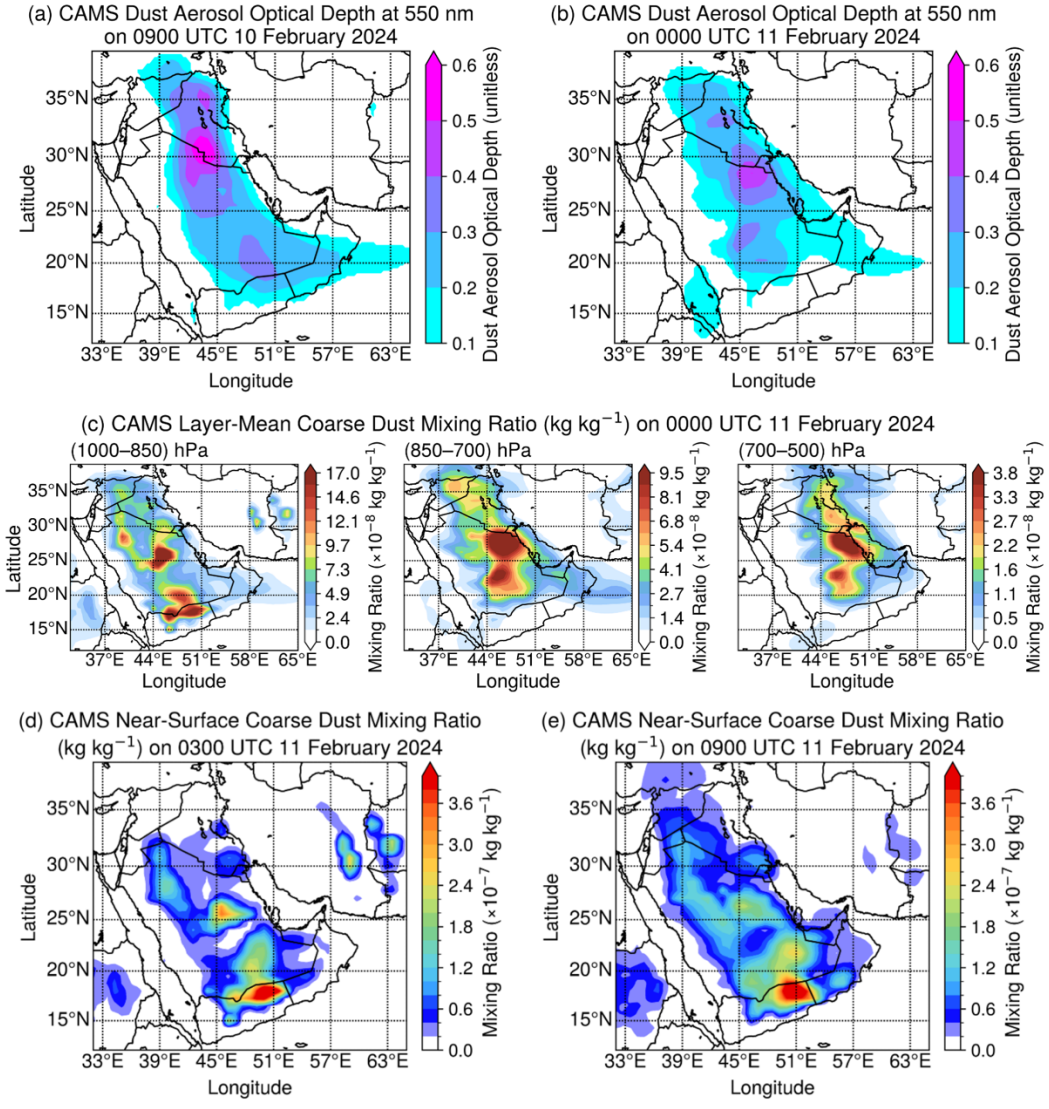

Figure 8. CAMS dust diagnostics for 10–12 February 2024 depicting (a–b) dust aerosol optical depth at 550 nm (dimensionless), (c) layer-mean coarse dust mixing ratio (kg kg⁻¹) within the 1000–850, 850–700, and 700–500 hPa layers at 0000 UTC 11 February, and (d–e) near-surface (1000 hPa) coarse dust mixing ratio (kg kg⁻¹) at 0300 and 0900 UTC 11 February, respectively, thereby characterizing the temporal evolution of the vertically extensive dust plume preceding and during the convective event.

During the nocturnal, hail-producing MCS, output from the CAMS reanalysis indicates only modest dust concentrations beneath the convective core and a pronounced reduction in aerosol loading within the mixed-phase region. In the absence of shortwave radiative forcing at night, and with the remaining dust plume largely advected away from the storm core, both aerosol–radiation and aerosol–cloud microphysical interaction pathways appear to have been weak. As a result, hail production

https://doi.org/10.5194/egusphere-2025-6305
Preprint. Discussion started: 12 January 2026

and storm sustenance during this interval were controlled primarily by dynamical and thermodynamic processes—specifically, pronounced upper-tropospheric divergence, deeply moist layers, strong vertical wind shear, and intense convective updrafts—rather than by dust-induced forcing. In the post-convective environment, the residual dust was restricted to a smaller, less vertically coherent plume over parts of southeastern AP, acting mainly as a passive tracer of the trailing airmass rather than as an active modulator of subsequent storm evolution.

3.6 Case focus: evolution of the hail-producing storm

The genesis and evolution of hailstorms can be attributed to pronounced convective instability within the atmospheric column, which supports deep cloud development extending into the mixed-phase and fully glaciated regions of the troposphere, thereby enhancing ice nucleation processes (Chevuturi et al., 2014). In addition, the combined analysis of polarimetric radar observables and thermodynamic profiles derived from radiosonde soundings has proven to be highly effective for characterizing the microphysical structure of hail-producing storms, particularly for the detection and classification of hail-related radar signatures.

In this study, the radar-derived storm object was selected on the basis of both spatial and temporal collocation with independently verified surface hail observations (Fig. 9a). This stringent matching procedure provides confidence that the radar-identified storm object was indeed associated with hailfall, thereby constraining the analysis to storm-scale dynamical and microphysical processes, as well as the ambient convective environment, that are directly conducive to hail formation. Specifically, radar-based storm tracks were systematically cross-referenced with ground-based hail reports to isolate the convective system responsible for the observed hail (Dixon & Wiener, 1993). This methodology ensures that the investigation focuses on radar-detected storm entities with confirmed hail production, rather than on polarimetric or reflectivity signatures that may not correspond to hail reaching the surface.

Utilizing radar-derived reflectivity centroid positions as reference points, in conjunction with the corresponding zonal (U) and meridional (V) wind components, a time-sequenced vector field was generated to characterize the temporal evolution of the storm (Fig. 9b). These maps provide a framework for assessing the bulk motion, orientation, and propagation speed of the convective system and allow for evaluation of the influence of environmental steering winds on distinct storm elements at varying altitudes within the troposphere. The resulting depiction traces the trajectory of the convective system from its initiation through the period of maximum hail production to its subsequent dissipation.

The HMA parameter (expressed in ktons) was visualized using a lower threshold of 100 ktons to isolate storm segments most likely associated with substantial hail production (Fig. 9c). Progressively more restrictive thresholds further refine the analysis to emphasize those portions of the storm most actively participating in hail generation. This threshold is interpreted as indicative of stronger updrafts capable of sustaining prolonged hydrometeor growth and lofting large volumes of hail. While hail can occur at lower HMA values, segments exceeding 100 ktons are more characteristic of organized, deep convective cores that are typically associated with high-impact hail events.

https://doi.org/10.5194/egusphere-2025-6305
Preprint. Discussion started: 12 January 2026

Given the inherent challenges associated with the direct detection of hail within convective storms (Chevuturi et al., 2014), numerous studies have introduced objective, radar-derived metrics and automated hail-detection algorithms that infer hail occurrence or potential from reflectivity patterns and vertical storm structure. For example, Abshaev (1999) developed a method to estimate HMA using C-band radar by combining the maximum reflectivity magnitude with the vertical extent of the 45 dBZ echo. This technique has been implemented operationally in hail suppression programs in Mendoza, Argentina, and Alberta, Canada, where it was integrated into the TITAN system for real-time application.

Building on foundational work such as that of Waldvogel et al. (1979), which demonstrated a strong relationship between the height of the 45 dBZ echo above the environmental freezing level (ΔH45) and surface hail observations, these operational frameworks have adopted threshold-based parameters, including Hail Mass and Vertically Integrated Hail Mass (VIHM), to quantify hail potential. Within this context, ΔH45 was identified as a primary predictor of hail probability and has consequently become a central component of many contemporary radar-based hail detection algorithms.

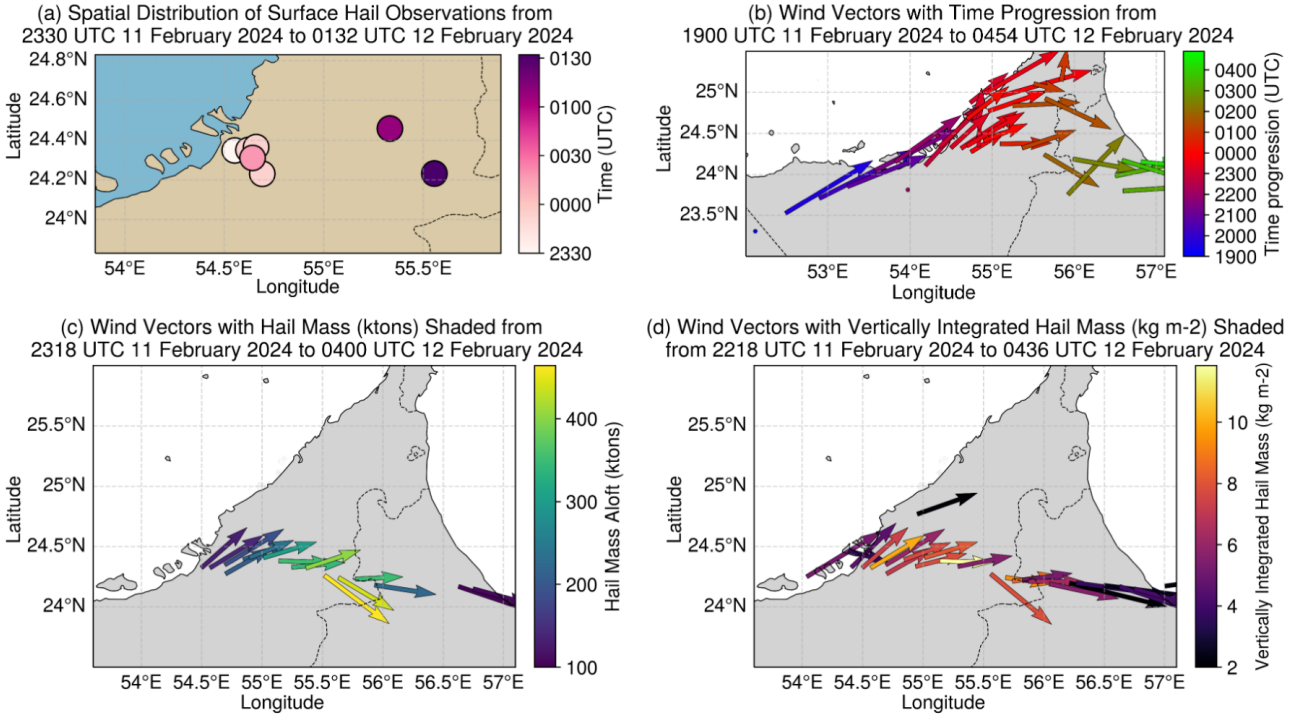

Figure 9. Spatial and temporal characteristics of the hail-producing storm over the UAE on 11–12 February 2024. (a) Confirmed surface hailfall reports. (b) Storm progression shown by wind vectors colored by time. (c) Wind vectors shaded by Hail Mass Aloft (HMA, ktons) highlighting segments with intense hail production. (d) Wind vectors shaded by Vertically Integrated Hail Mass (VIHM, kg/m²) indicating localized hail intensity.

Further validation and refinement of these techniques are presented by Foote et al. (2005), who evaluated these metrics during field campaigns conducted in Canada and Argentina. Their results corroborated that indices such as HMA and VIHM are not only highly responsive to hail growth processes in the mid- to upper levels of convective storms but also exhibit strong correspondence with damage reports and hailpad observations at the surface. They demonstrated that reflectivity values ≥ 60

https://doi.org/10.5194/egusphere-2025-6305
Preprint. Discussion started: 12 January 2026

dBZ aloft, in conjunction with peaks in VIHM, serve as robust indicators of severe hail, including in regions with complex orography. Moreover, their analysis supported the adoption of thresholds on the order of 100 ktons for HMA and 2 kg m^{-2} for VIHM as critical operational limits for discriminating potentially severe hail events (Donavon & Jungbluth, 2007). Collectively, these findings reinforce the thresholds employed in the present study and underscore their effectiveness in distinguishing hail-producing convective cells from weaker, non-severe convection, thereby enhancing the overall skill of severe weather forecasts, particularly in areas where direct hail observations are sparse or unavailable.

More importantly, the regions of elevated hail mass geographically coincided with areas where hailfall at the surface was independently verified by local emergency management agencies and storm spotter networks. This corroboration indicates that the proposed approach can diagnose a severe weather hazard, thereby reinforcing the utility of the indicator as a marker of hail-intensive storm phases. To ascertain whether the same storm segment was responsible for the observed surface hailfall, the VIHM field was examined (Fig. 9d). VIHM is derived from radar observations by vertically integrating hail mass throughout the storm column and expressing the result as an areal density. Its diagnostic value arises from the fact that a high HMA does not necessarily imply that hail reaches the surface. VIHM quantifies the degree to which hail mass is vertically concentrated in a configuration that enhances the probability of hailfall at the ground (Zhou et al., 2021). In the absence of vertical collocation and concentration of VIHM with respect to HMA, the storm is unlikely to generate intense, spatially focused hail cores.

To filter out marginal or weakly organized convection, a minimum VIHM threshold of 2 kg m^{-2} was applied, following Cintineo et al. (2012). This thresholding effectively eliminates less hazardous storms and restricts the analysis to the most intense and efficient hail producers. The resulting spatial distribution of VIHM closely resembled that of HMA, with VIHM maxima of 6–10 kg m^{-2} concentrated over the central and eastern UAE. These zones also coincided with regions where HMA exceeded 300–450 ktons, supporting the inference that this storm segment was the dominant contributor to the 12 February hailstorm event.

Figure 10a depicts storm depth (shaded), the altitude of maximum radar reflectivity (black line), and the corresponding reflectivity magnitudes (color-coded boxes). The time series is partitioned into three phases—initiation, peak, and dissipation—delimited by vertical red lines. These phase boundaries were defined subjectively to facilitate interpretation and do not result from an objective classification algorithm.

During several intervals, the cores of maximum reflectivity descended to substantially lower altitudes, followed by a period in which the reflectivity maxima were located higher aloft. This vertical displacement provides a plausible explanation for the discontinuity in surface hail reports. Hail was observed over Abu Dhabi and the surrounding region when the reflectivity maxima were located at relatively low levels, during which hailstones were likely to undergo substantial melting before reaching the surface, as well as earlier, when the reflectivity maxima were positioned at greater heights. Hail production resumed once the lower-level reflectivity cores became reestablished.

In the early stage of the event, reflectivity values were relatively weak and confined to the lower troposphere, indicative of modest convective intensity and the predominance of smaller hydrometeors (e.g., rain and graupel). The concurrent gradual

https://doi.org/10.5194/egusphere-2025-6305
Preprint. Discussion started: 12 January 2026

reduction in storm translation speed (Fig. 10b) is consistent with weak or poorly organized updrafts that had not yet fully coupled with the mid-tropospheric steering flow. As the updraft intensified and evolved into a mature, robust, and vertically extensive circulation—evidenced by an increase in storm volume and areal extent (Fig. 10c)—the system transitioned from scattered convection to a more organized and structured convective system.

Radar reflectivity values exceeding 65 dBZ became increasingly concentrated between approximately 2.5 km and 11 km AGL following the lofting of supercooled liquid water droplets above the freezing level by a strengthening updraft. This process promoted the development of deep, vertically oriented hail-generating cores. These reflectivity maxima were situated within the mixed-phase region of the cloud, where ice multiplication processes are most efficient and temperatures are near −10 °C, thereby enhancing the rapid transformation of graupel into hail. This configuration is indicative of an environment highly conducive to efficient hail growth.

Nelson (1983) demonstrated that hail production is favored in regions where substantial supercooled liquid water content coexists with strong updrafts within the mixed-phase layer, typically bounded by the 0 °C and −40 °C isotherms. Likewise, Rasmussen and Heymsfield (1987) emphasized the role of storm morphology and updraft kinematics in governing hailstone formation, growth, and residence time within this critical zone.

The 00 UTC OMAA radiosonde sounding (Fig. 6) provides thermodynamic context for these radar observations. The freezing level was located near 700 hPa, corresponding to approximately 3.3 km AGL. Most radar-derived reflectivity maxima were positioned well above this level, extending to nearly 11 km, further supporting the inference that hail growth was occurring primarily within the mixed-phase region. This layer spans temperatures of roughly 0 to −40 °C, with the most efficient hail growth typically occurring between −10 and −20 °C (Heymsfield, 1983; Heymsfield & Hjelmfelt, 1984).

The sounding additionally revealed a deep, moist mid-tropospheric layer and pronounced directional wind shear, conditions that are commonly associated with elevated convection and the formation of vertically coherent hail cores (Zhen et al., 2025). Taken together, these environmental characteristics are consistent with the radar-based evidence for a deep, well-organized convective storm structure during the period of peak hail production.

Two principal characteristics are evident in the storm's translational speed during this phase (Fig. 10b). Initially, the system experienced a rapid acceleration, which was subsequently followed by a quasi-steady propagation speed with only minor fluctuations. This abrupt increase in forward speed, concurrent with a rapid expansion in both storm volume and horizontal extent (Fig. 10c), is indicative of a period of explosive intensification, likely driven by strong cold-pool outflows and an enhanced dynamical coupling with the mid-tropospheric steering flow. The subsequent reduction in speed may reflect the storm's increasing proximity to land, which would partially restrict the low-level moisture flux from the Gulf. Alternatively, as the system migrated farther south, it may have encountered an environment less conducive to the efficient replacement of the upstream air mass. Either mechanism, or a combination of both, could have acted to decelerate the storm's forward motion despite the persistence of upper-level dynamical support.

https://doi.org/10.5194/egusphere-2025-6305
Preprint. Discussion started: 12 January 2026

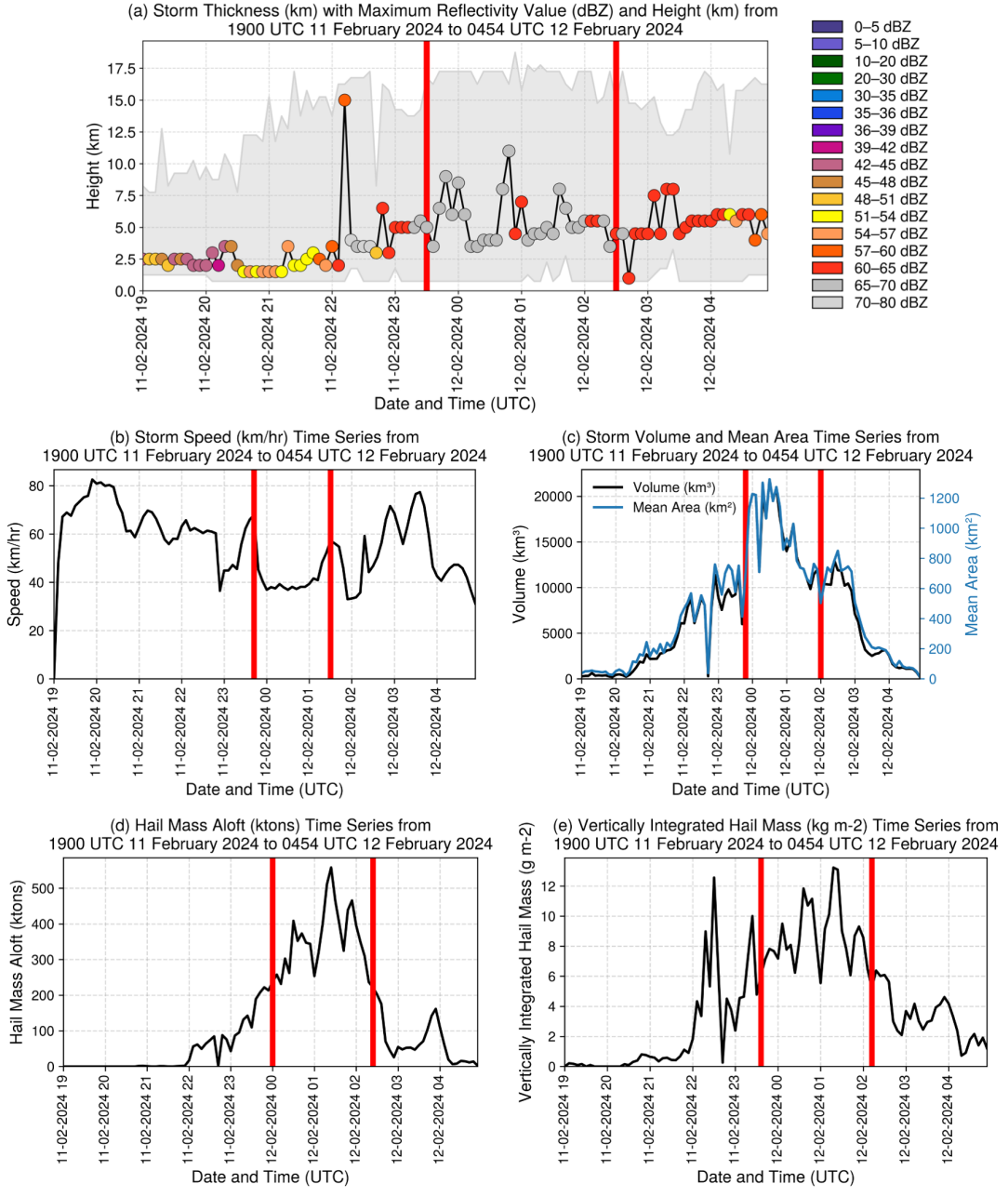

Figure 10. Time series of key storm characteristics from 1900 UTC 11 February to 0454 UTC 12 February 2024. (a) Storm thickness and height of maximum radar reflectivity (dBZ), with color-coded annotations. (b) Storm translational speed, illustrating a deceleration during the initiation phase and enhanced variability during the dissipation phase. (c) Storm volume (black) and mean horizontal area (blue), both attaining their maxima during the mature stage. (d) HMA and (e) VIHM, jointly emphasizing the efficiency of hail production within the storm. The vertical red lines delineate the approximate temporal boundaries of the initiation, mature, and dissipation phases of the storm. Because each parameter evolves on a slightly different timescale, the positions of these lines vary among panels to more accurately represent parameter-specific phase transitions.

https://doi.org/10.5194/egusphere-2025-6305
Preprint. Discussion started: 12 January 2026

Once established, the storm evolved into a mature stage characterized by a quasi-steady translational speed. During this phase, the storm volume and horizontal extent began to oscillate, reflecting the lifecycle of embedded hail cores within the organized convective system. These fluctuations are characteristic of a pulsing convective mode, in which robust upper-tropospheric forcing sustains deep convection through repeated cycles of hail core intensification and subsequent decay.

Both hail-related metrics exhibited strong and coherent signals during the peak phase of the storm (Figure 10d). HMA exceeded 500 ktons, indicative of substantial hail mass suspended within deep convective updrafts. Concurrently, VIHM displayed multiple sharp maxima, reaching values up to 12 kg m^{-2}, highlighting localized regions of particularly intense hail growth. The temporal evolution of these two parameters was closely aligned, with rapid increases followed by brief declines, consistent with the behavior of pulsing updrafts that strengthen, collapse, and then re-intensify. This pattern implies that hail production occurred in short-lived but vigorous episodes, each followed by partial weakening prior to the onset of the next cycle. The near-synchronous peaks in HMA and VIHM corroborate that this interval corresponded to the storm's period of maximum hail production efficiency and impact.

As the storm transitioned into a decaying phase, its forward motion became increasingly irregular (Fig. 10b), and both its volume and area displayed fluctuating yet overall decreasing trends (Fig. 10c). These variations point to a progressive loss of structural organization, likely associated with the development of downdrafts, interactions with the gust front, or splitting processes within the convective cells. During this stage, HMA decreased rapidly, and VIHM was characterized by irregular, low-magnitude peaks, indicative of intermittent and reduced hail formation (Fig. 10d). The weakening of the updrafts likely disrupted the storm's alignment with the mid-level steering flow, limiting further vertical development and ultimately contributing to its dissipation.

4 Discussion

The multi-source diagnostics (ECMWF-HRES, CAMS, Meteosat-9 Airmass RGB, OMAA radiosondes, and NCM radar) collectively indicate that the hail-producing event of 12 February 2024 was governed predominantly by synoptic-scale dynamical forcing. In this framework, moisture transport functioned as a necessary preconditioning factor, while atmospheric dust played a secondary role, primarily exerting a modulatory influence on the convective environment.

4.1 Physical mechanisms

The results indicate that storm development over the AP was strongly modulated by the JSP, which enhanced upper-tropospheric divergence and facilitated the amplification of PV anomalies (>9 PVU at 300 hPa; Fig. 2b), collocated with the coupled jet-streak structure (Fig. 2a). This, in turn, promoted the subsequent development and organization of the synoptic-scale system. This behavior is consistent with the established understanding that jet coupling sustains intense vertical motions and supports baroclinic growth during cyclogenesis. The event was characterized by a confluent configuration of a

https://doi.org/10.5194/egusphere-2025-6305
Preprint. Discussion started: 12 January 2026

polar cyclonic PV anomaly and a tropical anticyclonic PV anomaly, which sharpened the upper-tropospheric PV gradient, accelerated the jet, and intensified ageostrophic transverse circulations. This is evidenced by the juxtaposition of cyclonic and anticyclonic PV anomalies at 300 hPa (Fig. 2b) and the associated PV streamer structure apparent in the Airmass RGB imagery (Fig. 3).

The Airmass RGB signatures associated with dry stratospheric intrusions and PV streamer structures are consistent with previous investigations that have employed Airmass RGB as an upper-tropospheric dynamical diagnostic in Mediterranean cyclogenesis and severe-weather environments (Conte et al., 2011; Mavrakou & Cartalis, 2015), as well as with its operational application by NASA SPoRT and EUMETSAT (Berndt et al., 2014; Mavrakou & Cartalis, 2015). In the present case, the Airmass RGB imagery provided a qualitative depiction of the dynamical setting that supported the interpretation of the PV-driven environment, subsequently quantified using HRES PV and wind fields and documented in the Meteosat-9 Airmass RGB imagery (Fig. 3 and 7a–b).

A principal finding is that intense deep convection and associated hail developed within an environment characterized by extremely low CAPE (≈ 11.3 J kg^{-1} at 00 UTC, 12 February; Fig. 6), indicating that the absolute magnitude of buoyant instability alone did not govern storm severity. This contrasts with numerous midlatitude studies, in which large CAPE is frequently linked to significant hail production (Kaltenböck et al., 2009), and underscores that, in the hyper-arid United Arab Emirates, severe convective events can be controlled primarily by jet dynamics, moisture transport, and upper-tropospheric forcing rather than by buoyancy alone.

Moisture transport nevertheless remained a dominant controlling factor. Periods of weakened IVT coincided with diminished convective organization, whereas subsequent renewed moistening of the lower to mid-troposphere and an enhancement of vertical moisture continuity—evident in IVT diagnostics and in the OMAA sounding profile—were associated with convective re-intensification and MCS development over the AG and the UAE. This evolution is reflected by the pronounced decrease in IVT into the central AP (Fig. 5b), followed by renewed deep moistening in the OMAA sounding (Fig. 6). Temporal pulses in IVT were dynamically consistent with the evolution of the potential vorticity (PV) anomaly couplet, whereby southerly flow on the eastern flank of the cyclonic PV anomaly facilitated poleward moisture flux and sustained convection (Ralph et al., 2020).

CAMS analyses further indicate that mineral dust primarily acted as a secondary modulator of the evolving storm environment. This interpretation is supported by CAMS diagnostics, which show elevated dust AOD (≈ 0.5–0.6; Figure 8a–b) during the convective minimum, and substantially reduced dust loading beneath the nocturnal convective core (Fig. 8c–e). Dust-induced radiative stabilization may have contributed to the convective lull by enhancing mid-tropospheric static stability and strengthening capping inversions under conditions of reduced moisture transport.

In contrast, during the nocturnal hail-producing phase, dust concentrations within the convective core region remained relatively modest, and the pathways of aerosol–convection interaction appeared weak. Collectively, these results support the conclusion that hail production and storm persistence were controlled predominantly by dynamical and thermodynamic forcings, consistent with the diagnostic evidence presented in the Results. Maxima in HMA (> 500 ktons) and VIHM (> 12 kg

https://doi.org/10.5194/egusphere-2025-6305
Preprint. Discussion started: 12 January 2026

m^{-2}; Figs. 9–10) coincided with periods of enhanced upper-tropospheric divergence (Fig. 7b), underscoring the primary role of large-scale and mesoscale dynamics in governing storm intensity and hail formation.

4.2 Operational implications

Operationally, these findings suggest that forecasting and warning practices in the UAE should prioritize diagnostics of jet-stream coupling and PV streamer evolution, assessment of the continuity of moisture transport and the depth of tropospheric saturation, and the application of radar-based hail severity products, rather than relying predominantly on CAPE magnitude. The results demonstrate that radar-derived HMA and VIHM effectively captured the timing and spatial distribution of severe hail production and exhibited strong correspondence with verified surface hail reports, thereby supporting their operational utility for impact-oriented nowcasting in regions with sparse or limited surface observations.

4.3 Multi-source integration context

This paper presented a detailed analysis of the convective storm that affected the UAE on 12 February 2024, an anomalously intense hail-producing system for this climatologically hyper-arid region. The broader AP can be classified as hyper-arid, rendering this case a clear illustration of how large-scale dynamical forcing, in conjunction with a suitably conducive mesoscale environment, can override regional climatological norms to generate severe convective phenomena.

The numerical model outputs employed in this study are typically assimilated with data from remote-sensing platforms (e.g., Landsat-9, SEVIRI/MSG-3) and in situ observations (radiosondes), thereby providing optimized initial conditions for short-range forecasting (Cappelaere et al., 2020; Zhang et al., 2022). The model fields supply spatially and temporally continuous representations of the atmosphere, whereas the observations constrain and enhance the fidelity of key thermodynamic and dynamical structures. This model–observation integration is particularly critical in the UAE, where surface measurements are sparse, and it ensures that storm-scale analyses remain both physically consistent and firmly anchored in observations.

In contrast to the ERA5 reanalysis, which relies on a single, fixed model configuration throughout its temporal domain, the HRES forecast system is subject to continual updates and incorporates real-time observational data via data assimilation. The enhanced spatial and temporal resolution of the HRES dataset facilitates detailed characterization of mesoscale and synoptic environments, including phenomena such as dust transport (Heinold et al., 2013) and convection initiation.

Radiosonde observations were particularly critical for diagnosing atmospheric conditions conducive to deep convection. Nonetheless, due to the limited temporal sampling and restricted spatial representativeness of a single sounding station, model-derived fields from the ECMWF HRES system were employed in a complementary manner to refine analyses of the atmospheric state. Radiosonde measurements serve as the primary ground-truth constraint on the vertical thermodynamic and kinematic structure of the atmosphere. Unlike many numerical model outputs, they can resolve shallow temperature inversions, the vertical extent and layering of moisture, and vertical wind shear, all of which are often smoothed or inadequately represented in simulations. These high-vertical-resolution profiles constitute the principal reference for diagnosing jet-level

https://doi.org/10.5194/egusphere-2025-6305
Preprint. Discussion started: 12 January 2026

forcing and IVT, and they corroborate that the observed severe convection occurred in a low-CAPE environment dominated by strong dynamical forcing.

In studies where high-frequency and spatially dense radiosonde observations are impractical or unavailable, forecast model products provide valuable supplementary information. Although radiosondes yield highly accurate vertical profiles, their launch schedule (typically twice daily) and sparse spatial coverage limit their ability to capture rapidly evolving pre-convective environments. As a result, key features such as short-lived moisture surges, boundary-layer destabilization, or mesoscale convergence zones may go undetected (Merino et al., 2013). Brimelow et al. (2006) and Haklander and Van Delden (2003) underscored the challenges of relying solely on individual soundings to elucidate the mechanisms governing convective initiation. To address these limitations, Sánchez et al. (2009) emphasized the importance of augmenting radiosonde-derived diagnostics with forecast-based information, including mesoscale low-pressure systems, convergence lines, and other synoptically favorable configurations.

Numerous studies have demonstrated the utility of the Airmass RGB composite for the analysis of upper-tropospheric and lower-stratospheric dynamical processes. For instance, Conte et al. (2011) monitored the evolution of dry stratospheric intrusions associated with a Mediterranean cyclogenesis event, while Mavrakou and Cartalis (2015) employed Airmass RGB imagery to identify upper-level PV anomalies linked to severe weather occurrences over Europe. Both NASA SPoRT and EUMETSAT, as operational entities, routinely exploit Airmass RGB products to derive synoptic-scale diagnostics, including applications for tracking winter extratropical cyclones over North America and hail-producing convective systems in Central and Eastern Europe (Berndt et al., 2014; Bocheva et al., 2018).

These qualitative diagnostic applications underscore the capacity of Airmass RGB to elucidate atmospheric processes that are not fully resolved by radiosonde observations or numerical model output alone and are particularly advantageous in regions characterized by sparse observational networks. As an additional example, Kaltenböck et al. (2009) examined various instability indices from ECMWF forecast products over Europe, finding that CAPE values exceeding 400 J kg^{-1} were consistently associated with severe, hail-producing convection.

In the present study, ECMWF-derived CAPE fields were not explicitly plotted; however, the 00 UTC Abu Dhabi radiosonde on 12 February indicated a very low CAPE of 11.3 J kg^{-1}. This contrast highlights an important distinction: although elevated CAPE is frequently correlated with severe convective storms in midlatitude environments, the event under consideration was primarily governed by jet dynamics, moisture transport, and upper-level forcing, rather than by buoyant instability alone. This finding reinforces the limitations of CAPE as a standalone diagnostic for severe convection within the hyper-arid climatic regime of the UAE.

Similar methodological choices have been employed in numerous studies to address spatial observational gaps, whereby ECMWF-derived fields are incorporated to complement in situ and remote-sensing data when assessing atmospheric state variables and pre-convective environments, despite the inherent temporal and spatial constraints imposed by network coverage. Comparable applications of the ECMWF-HRES, used in conjunction with satellite observations, have demonstrated considerable skill in diagnosing high-impact weather events. Illustrative examples include analyses of the severe flooding that

https://doi.org/10.5194/egusphere-2025-6305
Preprint. Discussion started: 12 January 2026

affected Spain in September 2019 (Tapiador et al., 2021) and the extreme rainfall event that occurred in the United Arab Emirates in April 2024, investigated using an analogous dataset and methodological framework (AlShamsi et al., 2025).

5 Conclusion

The following conclusions are directly inferred from the multi-source results presented in Section 3, which synthesize ECMWF-HRES synoptic-scale diagnostics, Meteosat-9 Airmass RGB imagery interpretation, OMAA radiosonde thermodynamic and kinematic profiles, CAMS dust aerosol analyses, and hail-related metrics derived from NCM weather radar observations.

Evidence-based synthesis of principal findings: The synoptic-scale evolution during 10–12 February 2024 was governed by the superposition of the PJ and STJ, which enhanced upper-tropospheric divergence and facilitated the development and southeastward propagation of a COL. This configuration established persistent dynamical forcing for ascent over the AP and the UAE. Intrusions of high PV air and the associated baroclinic forcing contributed to cyclone intensification and the maintenance of a frontal zone that augmented low-level convergence, thereby creating a dynamically favorable environment for the initiation and organization of deep convection.

Moisture transport emerged as a critical enabling factor. IVT diagnostics and the OMAA sounding profile indicate that renewed moistening in the lower to middle troposphere, together with improved vertical continuity of moisture, coincided with convective regeneration and the transition toward an organized MCS impacting the AG and the UAE. The event occurred in a low-CAPE environment (OMAA CAPE ≈ 11.3 J kg^{-1}), implying that buoyant instability alone did not control convective intensity. Instead, the combined evidence supports a mechanism in which strong dynamical forcing and vertical wind shear, in conjunction with deep-layer moisture, facilitated elevated and organized convection capable of producing severe hail.

CAMS diagnostics suggest that mineral dust acted primarily as a secondary modulator of the evolving thermodynamic environment. During the nocturnal hail-producing phase, dust concentrations beneath the convective core were modest and the modeled aerosol–cloud interaction pathways were weak, reinforcing the interpretation that storm maintenance and hail production were dominated by dynamical and thermodynamic processes rather than aerosol effects. Radar-derived hail diagnostics, including the HMA and VIHM parameters, provided direct storm-scale evidence of severity, with their maxima collocated in space and time with the confirmed hail-producing storm segment as identified by surface hail reports.

These evidence-based findings support an operational focus on (i) monitoring jet–PV coupling and PV streamer evolution using HRES model diagnostics in conjunction with Airmass RGB imagery, (ii) characterizing moisture transport and vertical moisture continuity through IVT diagnostics and radiosonde profile analysis, and (iii) employing radar-derived hail metrics (HMA/VIHM) for real-time severe hail assessment and impact-oriented warning decision-making. A key subsequent priority is to expand event-based verification through the incorporation of additional surface hail observations and storm reports across the UAE, with the dual aims of refining region-specific hail-detection thresholds and quantifying uncertainty in radar-based hail retrievals under mixed-phase and high-attenuation conditions.

https://doi.org/10.5194/egusphere-2025-6305
Preprint. Discussion started: 12 January 2026

All conclusions articulated above are firmly anchored in the observational and modeling evidence detailed in the Results section and subsequently interpreted in the Discussion. This approach ensures that the overall synthesis remains consistent with the documented temporal evolution of the event and the associated diagnostic analyses.

Appendix A

Table A1. Confirmed surface hail observations employed for verification in Fig. 9a. The table enumerates each reporting site, including its geographic coordinates (longitude and latitude), together with the corresponding observation time in UTC during 11–12 February 2024.

Location	Longitude (° E)	Latitude (° N)	Date and Time
MBZ City	24.3478	54.5534	2331 UTC 11 Feb 2024
Al Wathba	24.2300	54.6915	2353 UTC 11 Feb 2024
Shakhbout City	24.3504	54.6224	2353 UTC 11 Feb 2024
Al Shawamekh	24.3650	54.6608	2353 UTC 11 Feb 2024
Bani Yas	24.3103	54.6429	0018 UTC 12 Feb 2024
Sweihan	24.4582	55.3324	0109 UTC 12 Feb 2024
Al Aamerah	24.2313	55.5559	0132 UTC 12 Feb 2024

Code availability. All codes used for the analysis and generating the figures can be obtained from the authors upon request.

Data availability. The ECMWF's "Atmospheric Model High-Resolution 10-day Forecast (Set I - HRES)" model output is publicly accessible at https://www.ecmwf.int/en/forecasts/datasets/set-i (accessed on 17 Dec 2025). CAMS "Copernicus Atmosphere Monitoring Service" global reanalysis dataset is publicly accessible at https://ads.atmosphere.copernicus.eu/datasets/cams-global-reanalysis-eac4 (accessed on 17 Dec 2025). EUMETSAT Meteosat-9 data can be accessed via the EUMETSAT Data Services: https://user.eumetsat.int/data-access/data-store (accessed on 17 Dec 2025). Other datasets are archived at the National Center of Meteorology of the United Arab Emirates and are available on request from the corresponding author. The data are not publicly available due to the policy of our project.

Author contributions. NA curated the data, performed the formal analysis and investigation, produced the visualizations, and wrote the initial draft. AAK, NA, and MW conceived the study; NA, MW, and AV developed the methodology. AAK administered the project, and AAM provided resources. AAK and MW validated the results. NA and MW revised the manuscript. All authors approved the final version.

Competing interests. The contact author has declared that none of the authors has any competing interests.

Acknowledgements. We acknowledge the European Centre for Medium-Range Weather Forecasts (ECMWF) for providing access to the Atmospheric Model High-Resolution 10-day Forecast (Set I – HRES) through their data server. We also thank

https://doi.org/10.5194/egusphere-2025-6305
Preprint. Discussion started: 12 January 2026

EUMETSAT for providing the Meteosat-9 (MSG-SEVIRI) observations used in this study. Additionally, we recognize the Climate Section of the National Center of Meteorology for supplying quality-controlled surface observations. The authors also acknowledge the continued institutional support of His Excellency Dr. Abdulla Al Mandous, President of the World Meteorological Organization (WMO) and Director General of the National Center of Meteorology, and Mr. Omar Al Yazeedi, Deputy Director General of the National Center of Meteorology.

The authors used an AI-based language editing tool solely to improve grammar and readability; All scientific ideas, analysis, and interpretations are entirely the work of the authors.

Financial support. This research received no external funding.

References

Abdullah, M., & Al-Mazroui, M. (1998). Climatological study of the southwestern region of Saudi Arabia. I. Rainfall analysis. *Climate Research*, *9*, 213–223. https://doi.org/10.3354/cr009213

Abshaev, M. T. (1999). Evolution of seeded and non seeded hailstorms. *Proc. Seventh WMO Scientific Conf. On Wea. Modification. WMP Report*, *31*, 407–410.

Airey, M. W., Nicoll, K. A., Harrison, R. G., & Marlton, G. J. (2021). Characteristics of desert precipitation in the UAE derived from a ceilometer dataset. *Atmosphere*, *12*(10). https://doi.org/10.3390/atmos12101245

Airmass RGB Quick Guide | EUMETSAT - User Portal. (n.d.). Retrieved July 24, 2025, from https://user.eumetsat.int/resources/user-guides/airmass-rgb-quick-guide

Allen, J. T., Giammanco, I. M., Kumjian, M. R., Jurgen Punge, H., Zhang, Q., Groenemeijer, P., Kunz, M., & Ortega, K. (2020). Understanding Hail in the Earth System. *Reviews of Geophysics*, *58*(1), e2019RG000665. https://doi.org/10.1029/2019RG000665;WGROUP:STRING:PUBLICATION

Almazroui, M., Awad, A. M., Islam, M. N., & Al-Khalaf, A. K. (2015). A climatological study: wet season cyclone tracks in the East Mediterranean region. *Theoretical and Applied Climatology*, *120*(1–2), 351–365. https://doi.org/10.1007/s00704-014-1178-z

Almazroui, M., Nazrul Islam, M., Athar, H., Jones, P. D., & Rahman, M. A. (2012). Recent climate change in the Arabian Peninsula: annual rainfall and temperature analysis of Saudi Arabia for 1978–2009. *International Journal of Climatology*, *32*(6), 953–966. https://doi.org/10.1002/joc.3446

AlShamsi, N., Kaabi, A. Al, Mandous, A. Al, Yazeedi, O. Al, Mazrouei, A. Al, Weston, M., VanderMerwe, A., Hussein, M., AlNaqbi, E., Kamali, A. Al, Farah, S., Ghafli, M. Al, & Maxwell, B. (2025). Synoptic-Scale Forcing and Its Role in a Rare Severe Rainfall Event over the UAE: A Case Study of 15–16 April 2024. *Atmosphere 2025, Vol. 16, Page 1267*, *16*(11), 1267. https://doi.org/10.3390/ATMOS16111267

https://doi.org/10.5194/egusphere-2025-6305
Preprint. Discussion started: 12 January 2026

Barbulescu, A., & Nazzal, Y. (2020). Statistical analysis of dust storms in the United Arab Emirates. *Atmospheric Research*, *231*, 104669. https://doi.org/10.1016/J.ATMOSRES.2019.104669

Beck, H. E., Zimmermann, N. E., McVicar, T. R., Vergopolan, N., Berg, A., & Wood, E. F. (2018). Present and future köppen-geiger climate classification maps at 1-km resolution. *Scientific Data*, *5*. https://doi.org/10.1038/sdata.2018.214

Berndt, E., Zavodsky, B., Molthan, A., Folmer, M., & Jedlovec, G. (2014). The Use of Red Green Blue (RGB) Air Mass Imagery to Investigate the Role of Stratospheric Air in a Non-Convective Wind Event. *EUMETSAT Meteorological Satellite Conference*, *M14-4012*.

Bhate, J., Kesarkar, A. P., Karipot, A., Bala Subrahamanyam, D., Rajasekhar, M., Sathiyamoorthy, V., & Kishtawal, C. M. (2016). A sea breeze induced thunderstorm over an inland station over Indian South Peninsula – A case study. *Journal of Atmospheric and Solar-Terrestrial Physics*, *148*, 96–111. https://doi.org/10.1016/J.JASTP.2016.09.002

Bocheva, L., Dimitrova, T., Penchev, R., Gospodinov, I., & Simeonov, P. (2018). Severe convective supercell outbreak over western Bulgaria on July 8, 2014. *Időjárás*, *122*(2).

Böer, B. (1997). An introduction to the climate of the United Arab Emirates. *Journal of Arid Environments*, *35*(1), 3–16. https://doi.org/10.1006/jare.1996.0162

Branch, O., Behrendt, A., Gong, Z., Schwitalla, T., & Wulfmeyer, V. (2020). Convection Initiation over the Eastern Arabian Peninsula. *Meteorologische Zeitschrift*, *29*(1), 67–77. https://doi.org/10.1127/metz/2019/0997

Brimelow, J. C., Reuter, G. W., Goodson, R., & Krauss, T. W. (2006). Spatial Forecasts of Maximum Hail Size Using Prognostic Model Soundings and HAILCAST. *Weather and Forecasting*, *21*(2), 206–219. https://doi.org/10.1175/WAF915.1

Brimelow, J. C., Reuter, G. W., & Poolman, E. R. (2002). Modeling Maximum Hail Size in Alberta Thunderstorms. *Weather and Forecasting*, *17*(5), 1048–1062. https://doi.org/10.1175/1520-0434(2002)017<1048:MMHSIA>2.0.CO;2

Cappelaere, B., Feurer, D., Vischel, T., Ottlé, C., Issoufou, H. B. A., Saux-Picart, S., Maïnassara, I., Oï, M., Chazarin, J. P., Barral, H., Coudert, B., & Demarty, J. (2020). Modeling Land Surface Fluxes from Uncertain Rainfall: A Case Study in the Sahel with Field-Driven Stochastic Rainfields. *Atmosphere 2020, Vol. 11, Page 465*, *11*(5), 465. https://doi.org/10.3390/ATMOS11050465

Chevuturi, A., Dimri, A. P., & Gunturu, U. B. (2014). Numerical simulation of a rare winter hailstorm event over Delhi, India on 17 January 2013. *Natural Hazards and Earth System Sciences*, *14*(12), 3331–3344. https://doi.org/10.5194/NHESS-14-3331-2014,

Christenson, C. E., Martin, J. E., & Handlos, Z. J. (2017). A synoptic climatology of Northern Hemisphere, cold season polar and subtropical jet superposition events. *J. Climate*, *30*, 7231–7246. https://doi.org/https://doi.org/10.1175/JCLI-D-16-0565.1

Cintineo, J. L., Smith, T. M., Lakshmanan, V., Brooks, H. E., & Ortega, K. L. (2012). An Objective High-Resolution Hail Climatology of the Contiguous United States. *Weather and Forecasting*, *27*(5), 1235–1248. https://doi.org/10.1175/WAF-D-11-00151.1

https://doi.org/10.5194/egusphere-2025-6305
Preprint. Discussion started: 12 January 2026

Conte, D., Miglietta, M. M., & Levizzani, V. (2011). Analysis of instability indices during the development of a Mediterranean tropical-like cyclone using MSG-SEVIRI products and the LAPS model. *Atmospheric Research*, *101*(1–2), 264–279. https://doi.org/10.1016/J.ATMOSRES.2011.02.016

Dasari, H. P., Desamsetti, S., Langodan, S., Attada, R., Ashok, K., & Hoteit, I. (2022). Long-term changes in the Arabian Peninsula rainfall and their relationship with the ENSO signals in the tropical Indo-Pacific. *Climate Dynamics*, *59*(5–6), 1715–1731. https://doi.org/10.1007/s00382-021-06062-7

DeHart, J., Dixon, M., Javornik, B., Bell, M., Cha, T.-Y., DesRosiers, A., & Lee, W.-C. (2024). *nsf-lrose/lrose-releases: lrose-colette-20240525*. Zenodo. https://doi.org/10.5281/zenodo.11510075

Delobbe, L., & Holleman, I. (2006). Uncertainties in radar echo top heights used for hail detection. *Meteorological Applications*, *13*(4), 361–374. https://doi.org/10.1017/S1350482706002374;PAGE:STRING:ARTICLE/CHAPTER

Deng, L., McCabe, M. F., Stenchikov, G., Evans, J. P., & Kucera, P. A. (2015). Simulation of Flash-Flood-Producing Storm Events in Saudi Arabia Using the Weather Research and Forecasting Model*. *Journal of Hydrometeorology*, *16*(2), 615–630. https://doi.org/10.1175/JHM-D-14-0126.1

Dixon, M., & Wiener, G. (1993). TITAN: Thunderstorm Identification, Tracking, Analysis, and Nowcasting—A Radar-based Methodology. *Journal of Atmospheric and Oceanic Technology*, *10*(6), 785–797. https://doi.org/10.1175/1520-0426(1993)010<0785:TTITAA>2.0.CO;2

Donavon, R. A., & Jungbluth, K. A. (2007). Evaluation of a Technique for Radar Identification of Large Hail across the Upper Midwest and Central Plains of the United States. *Weather and Forecasting*, *22*(2), 244–254. https://doi.org/10.1175/WAF1008.1

Farahat, A., El-Askary, H., & Al-Shaibani, A. (2015). Study of Aerosols' Characteristics and Dynamics over the Kingdom of Saudi Arabia Using a Multisensor Approach Combined with Ground Observations. *Advances in Meteorology*, *2015*. https://doi.org/10.1155/2015/247531

Fonseca, R., Francis, D., Nelli, N., Farrah, S., Wehbe, Y., Al Hosari, T., & Al Mazroui, A. (2022). Assessment of the WRF Model as a Guidance Tool Into Cloud Seeding Operations in the United Arab Emirates. *Earth and Space Science*, *9*(5). https://doi.org/10.1029/2022EA002269

Fonseca, R., Francis, D., Nelli, N., Yarragunta, Y., Paparella, F., & Pauluis, O. M. (2024). Summertime secondary convection and interaction with sea-breeze circulations. *Quarterly Journal of the Royal Meteorological Society*. https://doi.org/10.1002/qj.4907

Fonseca, R., Francis, D., Weston, M., Nelli, N., Farah, S., Wehbe, Y., AlHosari, T., Teixido, O., & Mohamed, R. (2021). Sensitivity of Summertime Convection to Aerosol Loading and Properties in the United Arab Emirates. *Atmosphere*, *12*(12), 1687. https://doi.org/10.3390/atmos12121687

Foote, G. B., Krauss, T. W., & Makitov, V. (2005). Hail metrics using conventional radar. *Proc., 16th Conference on Planned and Inadvertent Weather Modification*, 30.

https://doi.org/10.5194/egusphere-2025-6305
Preprint. Discussion started: 12 January 2026

Forcadell, V., Augros, C., Caumont, O., Dedieu, K., Ouradou, M., David, C., Figueras I Ventura, J., Laurantin, O., & Al-Sakka, H. (2024). Severe-hail detection with C-band dual-polarisation radars using convolutional neural networks. *Atmos. Meas. Tech*, *17*, 6707–6734. https://doi.org/10.5194/amt-17-6707-2024

Francis, D., Alshamsi, N., Cuesta, J., Gokcen Isik, A., & Dundar, C. (2019). Cyclogenesis and Density Currents in the Middle East and the Associated Dust Activity in September 2015. *Geosciences*, *9*(9), 376. https://doi.org/10.3390/geosciences9090376

Francis, D., Chaboureau, J. P., Nelli, N., Cuesta, J., Alshamsi, N., Temimi, M., Pauluis, O., & Xue, L. (2021). Summertime dust storms over the Arabian Peninsula and impacts on radiation, circulation, cloud development and rain. *Atmospheric Research*, *250*(July 2020), 105364. https://doi.org/10.1016/j.atmosres.2020.105364

Galarneau, T. J., Bosart, L. F., & Schumacher, R. S. (2010). Predecessor Rain Events ahead of Tropical Cyclones. *Monthly Weather Review*, *138*(8), 3272–3297. https://doi.org/10.1175/2010MWR3243.1

Gopalakrishnan, D., Taraphdar, S., Pauluis, O. M., Xue, L., Ajayamohan, R. S., Al Shamsi, N., Chen, S., Lee, J. A., Grabowski, W. W., Liu, C., Tessendorf, S. A., & Rasmussen, R. M. (2023). Anatomy of a Summertime Convective Event over the Arabian Region. *Monthly Weather Review*, *151*(4), 989–1004. https://doi.org/10.1175/MWR-D-22-0082.1

Haklander, A. J., & Van Delden, A. (2003). Thunderstorm predictors and their forecast skill for the Netherlands. *Atmospheric Research*, *67–68*, 273–299. https://doi.org/10.1016/S0169-8095(03)00056-5

Hamzeh, N. H., Karami, S., Kaskaoutis, D. G., Tegen, I., Moradi, M., & Opp, C. (2021). Atmospheric Dynamics and Numerical Simulations of Six Frontal Dust Storms in the Middle East Region. *Atmosphere 2021, Vol. 12, Page 125*, *12*(1), 125. https://doi.org/10.3390/ATMOS12010125

Han, L., Fu, S., Zhao, L., Zheng, Y., Wang, H., & Lin, Y. (2009). 3D convective storm identification, tracking, and forecasting—An enhanced TITAN algorithm. *Journal of Atmospheric and Oceanic Technology*, *26*(4), 719–732.

Heinold, B., Knippertz, P., Marsham, J. H., Fiedler, S., Dixon, N. S., Schepanski, K., Laurent, B., & Tegen, I. (2013). The role of deep convection and nocturnal low-level jets for dust emission in summertime West Africa: Estimates from convection-permitting simulations. *Journal of Geophysical Research: Atmospheres*, *118*(10), 4385–4400. https://doi.org/10.1002/jgrd.50402

Heymsfield, A. J. (1983). Case Study of a Halistorm in Colorado. Part IV: Graupel and Hail Growth Mechanisms Deduced through Particle Trajectory Calculations. *Journal of the Atmospheric Sciences*, *40*(6), 1482–1509. https://doi.org/10.1175/1520-0469(1983)040<1482:CSOAHI>2.0.CO;2

Heymsfield, A. J., & Hjelmfelt, M. R. (1984). Processes of Hydrometeor Development in Oklahoma Convective Clouds. *Journal of the Atmospheric Sciences*, *41*(19), 2811–2835. https://doi.org/10.1175/1520-0469(1984)041<2811:POHDIO>2.0.CO;2

Houssos, E. E., Chronis, T., Fotiadi, A., & Hossain, F. (2015). Atmospheric Circulation Characteristics Favoring Dust Outbreaks over the Solar Village, Central Saudi Arabia*. *Monthly Weather Review*, *143*(8), 3263–3275. https://doi.org/10.1175/MWR-D-14-00198.1

https://doi.org/10.5194/egusphere-2025-6305
Preprint. Discussion started: 12 January 2026

Hulton, F., & Schultz, D. M. (2024). Climatology of large hail in Europe: Characteristics of the European Severe Weather Database. *Natural Hazards and Earth System Sciences*, *24*(4), 1079–1098. https://doi.org/10.5194/NHESS-24-1079-2024,

Husain, T., & Chaudhary, J. R. (2008). Human Health Risk Assessment due to Global Warming – A Case Study of the Gulf Countries. *International Journal of Environmental Research and Public Health*, *5*(4), 204–212. https://doi.org/10.3390/ijerph5040204

Inness, A., Ades, M., Agustí-Panareda, A., Barr, J., Benedictow, A., Blechschmidt, A. M., Jose Dominguez, J., Engelen, R., Eskes, H., Flemming, J., Huijnen, V., Jones, L., Kipling, Z., Massart, S., Parrington, M., Peuch, V. H., Razinger, M., Remy, S., Schulz, M., & Suttie, M. (2019). The CAMS reanalysis of atmospheric composition. *Atmospheric Chemistry and Physics*, *19*(6), 3515–3556. https://doi.org/10.5194/ACP-19-3515-2019

Kaltenböck, R., Diendorfer, G., & Dotzek, N. (2009). Evaluation of thunderstorm indices from ECMWF analyses, lightning data and severe storm reports. *Atmospheric Research*, *93*(1–3), 381–396. https://doi.org/10.1016/J.ATMOSRES.2008.11.005

Kopp, J., Hering, A., Germann, U., & Martius, O. (2024). Verification of weather-radar-based hail metrics with crowdsourced observations from Switzerland. *Atmospheric Measurement Techniques*, *17*(14), 4529–4552. https://doi.org/10.5194/AMT-17-4529-2024,

Kumar, K. N., Entekhabi, D., & Molini, A. (2015). Hydrological extremes in hyperarid regions: A diagnostic characterization of intense precipitation over the Central Arabian Peninsula. *Journal of Geophysical Research: Atmospheres*, *120*(5), 1637–1650. https://doi.org/10.1002/2014JD022341

Kunz, M., Sander, J., & Kottmeier, C. (2009). Recent trends of thunderstorm and hailstorm frequency and their relation to atmospheric characteristics in southwest Germany. *International Journal of Climatology*, *29*(15), 2283–2297. https://doi.org/10.1002/JOC.1865

Kunz, M., Wandel, J., Fluck, E., Baumstark, S., Mohr, S., & Schemm, S. (2020). Ambient conditions prevailing during hail events in central Europe. *Natural Hazards and Earth System Sciences*, *20*(6), 1867–1887. https://doi.org/10.5194/NHESS-20-1867-2020,

Marsham, J. H., & Ryder, C. L. (2021). Dust storms and haboobs. *Weather*, *76*(11), 378–379. https://doi.org/10.1002/WEA.4071

Mavrakou, T., & Cartalis, C. (2015). *An assessment of the potential of earth observation data to detect and monitor storm cells associated with natural hazards – an application to an extreme weather event in southeastern Mediterranean*. https://doi.org/10.5194/NHESSD-3-2191-2015

Mazza, E., Ulbrich, U., & Klein, R. (2017). The Tropical Transition of the October 1996 Medicane in the Western Mediterranean Sea: A Warm Seclusion Event. *Monthly Weather Review*, *145*(7), 2575–2595. https://doi.org/10.1175/MWR-D-16-0474.1

Merino, A., García-Ortega, E., López, L., Sánchez, J. L., & Guerrero-Higueras, A. M. (2013). Synoptic environment, mesoscale configurations and forecast parameters for hailstorms in Southwestern Europe. *Atmospheric Research*, *122*, 183–198. https://doi.org/10.1016/J.ATMOSRES.2012.10.021

https://doi.org/10.5194/egusphere-2025-6305
Preprint. Discussion started: 12 January 2026

Miller, S. D., Kuciauskas, A. P., Liu, M., Ji, Q., Reid, J. S., Breed, D. W., Walker, A. L., & Mandoos, A. Al. (2008). Haboob dust storms of the southern Arabian Peninsula. *Journal of Geophysical Research: Atmospheres*, *113*(D1). https://doi.org/10.1029/2007JD008550

Mohammed Abdul Raheem Jabbar, & Ahmad S. Hassan. (2022). A Cut-off low at 500 hPa Geopotential Height and Rainfall Events over Iraq: Case Studies. *Iraqi Journal of Physics*, *20*(3), 76–85. https://doi.org/10.30723/ijp.v20i3.1007

Molthan, A. L., Fuell, K. K., Oswald, H. K., & Knaff, J. A. (2012). *Development of RGB Composite Imagery for Operational Weather Forecasting Applications*.

Nakamura, H., Sampe, T., Tanimoto, Y., & Shimpo, A. (2004). Observed associations among storm tracks, jet streams and midlatitude oceanic fronts. *Geophysical Monograph Series*, *147*, 329–345. https://doi.org/10.1029/147GM18;CSUBTYPE:STRING:EDITED

Nazzal, Y., Barbulescu, A., Howari, F., Yousef, A., Al-Taani, A. A., Al Aydaroos, F., & Naseem, M. (2019). New insights on sand dust storm from historical records, UAE. *Arabian Journal of Geosciences*, *12*(13), 1–11. https://doi.org/10.1007/S12517-019-4555-1/METRICS

Nelli, N. R., Francis, D., Fonseca, R., Abida, R., Weston, M., Wehbe, Y., & Al Hosary, T. (2021). The atmospheric controls of extreme convective events over the southern Arabian Peninsula during the spring season. *Atmospheric Research*, *262*, 105788. https://doi.org/10.1016/j.atmosres.2021.105788

Nelson, S. P. (1983). The Influence of Storm Flow Structure on Hail Growth. *Journal of the Atmospheric Sciences*, *40*(8), 1965–1983. https://doi.org/10.1175/1520-0469(1983)040<1965:TIOSFS>2.0.CO;2

Olivares, L., & Jordan, T. E. (2024). Contributions by extreme rain events to long-term hyperarid landscape evolution. *Quaternary Science Reviews*, *332*, 108658. https://doi.org/10.1016/j.quascirev.2024.108658

Palmén, E., & Newton, C. W. (1969). *Atmospheric Circulation Systems: Their Structure and Physical Interpretation*.

Patlakas, P., Stathopoulos, C., Flocas, H., Kalogeri, C., & Kallos, G. (2019). Regional Climatic Features of the Arabian Peninsula. *Atmosphere*, *10*(4), 220. https://doi.org/10.3390/atmos10040220

Pilorz, W., & Łupikasza, E. (2020). Radar reflectivity signatures and possible lead times of warnings for very large hail in Poland based on data from 2007-2015. *Environmental & Socio-Economic Studies*, *8*(3), 34–47.

Ragab, R., & Prudhomme, C. (2000). Climate change and water resources management in the southern Mediterranean and Middle East countries. *The Second World Water Forum*, 17–22.

Ralph, F. M., Dettinger, M. D., Rutz, J. J., & Waliser, D. E. (2020). Atmospheric Rivers. *Atmospheric Rivers*, 1–252. https://doi.org/10.1007/978-3-030-28906-5/COVER

Rasmussen, R. M., & Heymsfield, A. J. (1987). Melting and Shedding of Graupel and Hail. Part III: Investigation of the Role of Shed Drops as Hail Embryos in the 1 August CCOPE Severe Storm. *Journal of the Atmospheric Sciences*, *44*(19), 2783–2803. https://doi.org/10.1175/1520-0469(1987)044<2783:MASOGA>2.0.CO;2

https://doi.org/10.5194/egusphere-2025-6305
Preprint. Discussion started: 12 January 2026

Raupach, T. H., Martynov, A., Nisi, L., Hering, A., Barton, Y., & Martius, O. (2021). Object-based analysis of simulated thunderstorms in Switzerland: Application and validation of automated thunderstorm tracking with simulation data. *Geoscientific Model Development*, *14*(10), 6495–6514. https://doi.org/10.5194/GMD-14-6495-2021,

Riemer, M., & Montgomery, M. T. (2011). Simple kinematic models for the environmental interaction of tropical cyclones in vertical wind shear. *Atmospheric Chemistry and Physics*, *11*(17), 9395–9414. https://doi.org/10.5194/ACP-11-9395-2011,

Sánchez, J. L., Marcos, J. L., Dessens, J., López, L., Bustos, C., & García-Ortega, E. (2009). Assessing sounding-derived parameters as storm predictors in different latitudes. *Atmospheric Research*, *93*(1–3), 446–456. https://doi.org/10.1016/J.ATMOSRES.2008.11.006

Saqer, R., Issa, S., & Saleous, N. (2024). Spatio-temporal characterization of PM10 concentration across Abu Dhabi Emirate (UAE). *Heliyon*, *10*, e32812. https://doi.org/10.1016/j.heliyon.2024.e32812

Schwitalla, T., Branch, O., & Wulfmeyer, V. (2020). Sensitivity study of the planetary boundary layer and microphysical schemes to the initialization of convection over the Arabian Peninsula. *Quarterly Journal of the Royal Meteorological Society*, *146*(727), 846–869. https://doi.org/10.1002/qj.3711

Solomos, S., Ansmann, A., Mamouri, R. E., Binietoglou, I., Patlakas, P., Marinou, E., & Amiridis, V. (2017). Remote sensing and modelling analysis of the extreme dust storm hitting the Middle East and eastern Mediterranean in September 2015. *Atmospheric Chemistry and Physics*, *17*(6), 4063–4079. https://doi.org/10.5194/ACP-17-4063-2017

Steinhoff, D. F., Bruintjes, R., Hackera, J., Keller, T., Williams, C., Jensen, T., Al Mandous, A., & Al Yazeedi, O. A. (2018). Influences of the Monsoon Trough and Arabian Heat Low on Summer Rainfall over the United Arab Emirates. *Monthly Weather Review*, *146*(5), 1383–1403. https://doi.org/10.1175/MWR-D-17-0296.1

Tapiador, F. J., Marcos, C., Sancho, J. M., Santos, C., Núñez, J. Á., Navarro, A., Kummerow, C., & Adler, R. F. (2021). The September 2019 floods in Spain: An example of the utility of satellite data for the analysis of extreme hydrometeorological events. *Atmospheric Research*, *257*, 105588. https://doi.org/10.1016/J.ATMOSRES.2021.105588

Thompson, C. F., Schultz, D. M., & Vaughan, G. (2018). A Global Climatology of Tropospheric Inertial Instability. *Journal of the Atmospheric Sciences*, *75*(3), 805–825. https://doi.org/10.1175/JAS-D-17-0062.1

Trenberth, K. E., & Shea, D. J. (2005). Relationships between precipitation and surface temperature. *Geophysical Research Letters*, *32*(14), 1–4. https://doi.org/10.1029/2005GL022760;PAGEGROUP:STRING:PUBLICATION

Tsironis, A., Cartalis, C., & Flocas, H. (2023). Use of Satellite-Based Indicators to Study the Role of Jet Stream Superposition on High-Impact Weather Events in the Mediterranean Region. *16th International Conference on Meteorology, Climatology and Atmospheric Physics—COMECAP 2023*, 134. https://doi.org/10.3390/environsciproc2023026134

Waldvogel, A., Federer, B., & Grimm, P. (1979). Criteria for the Detection of Hail Cells. *Journal of Applied Meteorology and Climatology*, *18*(12), 1521–1525. https://doi.org/10.1175/1520-0450(1979)018<1521:CFTDOH>2.0.CO;2

Winters, A. C., & Martin, J. E. (2016). Synoptic and mesoscale processes supporting vertical superposition of the polar and subtropical jets in two contrasting cases. *Quart. J. Roy. Meteor. Soc.*, *142*, 1133–1149. https://doi.org/https://doi.org/10.1002/qj.2718

https://doi.org/10.5194/egusphere-2025-6305
Preprint. Discussion started: 12 January 2026

Yamane, Y., & Hayashi, T. (2006). Evaluation of environmental conditions for the formation of severe local storms across the Indian subcontinent. *Geophysical Research Letters*, *33*(17), 17806. https://doi.org/10.1029/2006GL026823;SUBPAGE:STRING:FULL

Yang, D., Wang, W., & Hong, T. (2022). A historical weather forecast dataset from the European Centre for Medium-Range Weather Forecasts (ECMWF) for energy forecasting. *Solar Energy*, *232*, 263–274. https://doi.org/10.1016/J.SOLENER.2021.12.011

Yousef, L. A., Temimi, M., Wehbe, Y., & Al Mandous, A. (2019). Total cloud cover climatology over the United Arab Emirates. *Atmospheric Science Letters*, *20*(2). https://doi.org/10.1002/asl.883

ZAVODSKY, B. T., MOLTHAN, A. L., & FOLMER, M. J. (2013). Multispectral Imagery for Detecting Stratospheric Air Intrusions Associated with Mid-Latitude Cyclones. *Journal of Operational Meteorology*, *1*(7).

Zhang, L., Montuoro, R., McKeen, S. A., Baker, B., Bhattacharjee, P. S., Grell, G. A., Henderson, J., Pan, L., Frost, G. J., McQueen, J., Saylor, R., Li, H., Ahmadov, R., Wang, J., Stajner, I., Kondragunta, S., Zhang, X., & Li, F. (2022). Development and evaluation of the Aerosol Forecast Member in the National Center for Environment Prediction (NCEP)'s Global Ensemble Forecast System (GEFS-Aerosols v1). *Geoscientific Model Development*, *15*(13), 5337–5369. https://doi.org/10.5194/GMD-15-5337-2022,

Zhen, X., Chen, H., Shi, H., Fan, X., Chen, H., Fu, J., Wei, W., Ma, S., Yang, L., & He, J. (2025). A Case Study of a Hailstorm in the Shanghai Region: Leveraging Multisource Observational Data and a Novel Single-Polarization X-Band Array Weather Radar. *Sensors 2025, Vol. 25, Page 2870*, *25*(9), 2870. https://doi.org/10.3390/S25092870

Zhou, Z., Zhang, Q., Allen, J. T., Ni, X., & Ng, C. P. (2021). How Many Types of Severe Hailstorm Environments Are There Globally? *Geophysical Research Letters*, *48*(23), e2021GL095485. https://doi.org/10.1029/2021GL095485